Summer 2002

Excimer Emission From Pulsed Microhollow Cathode Discharges

Mohamed Moselhy
Old Dominion University

EXCIMER EMISSION FROM PULSED MICROHOLLOW

CATHODE DISCHARGES

by

Mohamed Moselhy
B.Sc. June 1993, University of Alexandria, Egypt
M.Sc. November 1997, University of Alexandria, Egypt

A Dissertation Submitted to the Faculty of
Old Dominion University in Partial Fulfillment of the
Requirement for the Degree of

DOCTOR OF PHILOSOPHY

ELECTRICAL ENGINEERING

OLD DOMINION UNIVERSITY
August 2002

Approved by:

_____
Karl H. Schoenbach (Director)

_____
Hani E. Elsayed-Ali (Member)

_____
Ravindra P. Joshi (Member)

_____
Leposava Vuskovic (Member)

ABSTRACT

EXCIMER EMISSION FROM PULSED MICROHOLLOW CATHODE DISCHARGES

Mohamed Moselhy
Old Dominion University, 2002
Director: Dr. Karl H. Schoenbach

Microhollow cathode discharges (MHCDs) are direct current, high-pressure, non-equilibrium gas discharges. Direct current MHCDs in xenon and argon have shown to emit excimer radiation at 172 and 127 nm, respectively. Internal efficiency of excimer emission in DC MHCD was measured to be 6-9% in xenon, and 1-6%, depending on the gas flow rate in argon. This high efficiency is due to the high rate of rare gas excitation by electrons accelerated in the cathode fall and to subsequent three-body collisions in the high-pressure gas. The excimer power scales linearly with current; however, due to the increasing size of the source with increasing current, the radiant emittance and the current density stay constant at 1.5 W/cm^2 and 0.3 A/cm^2, respectively, at 400 Torr xenon. In DC operation, the current was limited to 8 mA to avoid thermal damage of the electrodes. In order to explore the discharge physics and the excimer emission at higher currents, the discharge was pulsed with a duty cycle of 0.0007. This allowed us to increase the peak power and current without increasing the average power. A discharge behavior different from the DC and quasi DC (ms pulsed) was observed when the pulse was reduced to values in the order of the electron relaxation time. For argon this is in the order of 36 ns at atmospheric

pressure. Pulsing the discharge with such short pulses allows for heating the electrons without heating the gas. Applying electrical pulses of 20 ns duration to direct current MHCDs in xenon increased the excimer emission exponentially with the pulse voltage by more than two orders of magnitude over the DC value. At 750 V pulse voltage, an output VUV optical power of 2.75 W and internal efficiency of 20% was measured. Pulsing MHCDs in argon with a 10 ns pulse increased the intensity by a factor of six but the efficiency was not increased beyond the DC value. Electron density measurements using the Stark effect showed that the increase in excimer intensity was due to the increase in electron density and the increased electron energy caused by pulsed electron heating.

ACKNOWLEDGMENTS

I would like first to thank God for giving me the ability to accomplish my goal. I would like to thank my advisor, Dr. Karl H. Schoenbach, for his guidance and continuous support throughout this research and graduate study. I would like to thank Dr. Leposava Vuskovic, Dr. Hani E. Elsayed-Ali, and Dr. Ravindra P. Joshi for serving on my dissertation committee. I also would like to thank all the ECE faculty and staff.

I am very grateful for the valuable discussions with Dr. Ahmed El-Habachi, Dr. Frank Liepold, Dr. Juergen Kolb, Sunao Katsuki, and Dr. Susumu Kono. I also would like to thank Abdel-Aleam Mohamed, Wenhui shi, Chunqi Jiang, Shu Xiao and Ron Bentley for their help during the course of this dissertation.

I thank Tamer Refaat, Amr Abou-Ghazala, Ibrahim El-Kholy, and many others for their friendship and encouragement during my study.

Finally, I would like to thank my parents for their belief in me and for their love and my sister for her friendship and support during the completion of my dissertation.

TABLE OF CONTENTS

Chapter   Page

LIST OF TABLES

LIST OF FIGURES

CHAPTER I

INTRODUCTION

An excimer lamp is a quasi-monochromatic ultraviolet (UV) light source emitting in a narrow wavelength range. This has been achieved by forming a gas discharge either in rare gases or rare gas halides [1-7]. Excimer lamps can be operated in DC, pulsed, RF, or externally pumped by an electron beam mode. The advantages of these lamps are mercury free operation, high efficiency, and no radiation in the infrared range, which make them suitable for processes requiring low operating temperatures [8]. Excimer lamps are used for ultraviolet (UV) curing, photolithography, pollution control, ozone generation, material deposition, and plasma panel displays. Different configurations have been utilized for excimer lamps such as dielectric barrier discharge, corona discharge, microwave discharge, and microhollow cathode discharge geometries and have been studied for over two decades.

UV and Vacuum Ultraviolet (VUV) radiation are currently considered two of the main tools for many applications since UV and VUV lamps, which do not generate harmful products, are environmentally clean. In addition, UV lamps have a low cost compared to other UV and VUV, sources such as excimer lasers. Applications that use UV radiation require large area processing, which can be achieved easily in many of the available UV sources. Examples of these applications are UV sterilization, UV lithography, UV curing, dye laser pumping, and photodecomposition. These applications require an efficient, high intensity

---

The journal model for this thesis is *Applied Physics Letters*.

emission in a narrow wavelength range, which is available in excimer lamps.

UV lamps can be classified in different ways according to intensity, efficiency, output power, or emission spectrum. The emission spectrum of a UV lamp can be categorized into three main categories: a) line emission emitted by mercury lamps, b) broadband emission emitted by xenon arc lamps, and c) excimer emission lamps generated by dielectric barrier discharges, corona discharges, and microhollow cathode discharges.

Mercury lamps are low-pressure glow discharges, which have line emissions in a wide range from 184.9 nm to 579 nm. One of the most widely used models in laboratory spectrometry calibration is the Pen-Ray mercury lamp. This lamp is characterized by its high efficiency of the 253.7 nm line emission that reaches up to 70% and has a power density ranging from 40 $\mu W/cm^2$ to 20 mW/cm^2 [9]. Direct exposure to these lamps causes injury to the skin and eyes so covering a mercury lamp with a phosphor layer would convert the UV radiation into visible radiation that can be used for lighting purposes.

A short arc lamp is an example for a broad emission spectrum lamp. It is generally a spherical or slightly oblong quartz bulb with two electrodes separated by a few millimeters gap in which an arc is formed. The bulb is filled either with xenon, mercury vapor, or a mixture of both at high pressure. The output power is anywhere from a few hundred watts to a few kilowatts. With the small arc size and this amount of power, the arc is extremely intense; therefore, short arc lamps are usually used in movie theater projectors, searchlights, specialized medical equipment with fiber optic light delivery means, and some scientific equipment

requiring an extremely intense light source. The emission range depends on the gas mixture used. For example, in xenon short arc lamps the emission extends from deep UV (below 300 nm) to infrared; the spectrum is continuous, with near infrared xenon lines more significant, which detract from the efficiency at which visible light can be produced. The high cost, short lifetime, and limited efficiency (1%) due to electrode losses make short arc lamps impractical for general-purpose lighting [10].

Different configurations have been used in excimer lamps. Dielectric Barrier discharges (DBDs) are of the most common excimer discharges. They are also referred to as silent discharges and are non-equilibrium gas discharge that can be operated in a wide pressure range from 0.1 to 10 bar. They had been mainly used for ozone and nitrogen oxide generation but recently have also been used for UV excimer generation in excimer lamps, flue gas treatments, surface modification, and pollution control. Their main advantage is large gas flow operation at atmospheric pressure, which can be used with non-equilibrium plasma conditions. DBDs are characterized by the presence of at least one insulating layer in contact with the discharge between two plane or cylindrical electrodes. This is mainly a capacitor configuration in which an RF power supply is used. When applying the voltage, a displacement current flows through the dielectric and a space charge is accumulated on the dielectric surface. As a result of this space charge, the electric field is intensified and a breakdown occurs. An atmospheric pressure electrical breakdown in such a dielectric barrier configuration occurs in a large number of statistically distributed microdischarges

over the surface of the dielectric. The normal appearance of the discharge consists of a number of short-lived current filaments, with a duration of about 100 ns or less, referred to as microdischarges. Each discharge is an almost cylindrical weakly ionized plasma channel with a radius of about 100 μm and spreads into a large surface discharge at the dielectric surface. When the voltage is applied to the DBD configuration, the electric field initiates a local breakdown in the gap. Electrons generated by the breakdown while propagating in the gap will avalanche producing a high space charge, and hence, self-propagating streamers are generated.

Kogelschatz has studied various gases for UV excimer radiation in DBD such as argon (Ar), xenon (Xe), and xenon chloride (XeCl) and has calculated the efficiency of UV generation in xenon as a function of the reduced electric field (E/n) [11]. Based on these calculations, a maximum efficiency of 40 % for a reduced electric field range of 40-120 Td ($Td=10^{-17}$ V cm^2) can be expected. This range of reduced electric field provides both the required electron energy and density for an efficient excimer generation since higher electron density would result in quenching the excimer states by electronic collisions, which will reduce the efficiency. Recently, Mildren and Carman used short-pulse excitation with DBD lamps [12]. In their measurements they found that, due to this pulsed excitation, the efficiency increased by about 12 % with respect to the RF operation efficiency.

In the microwave region (0.3-10 GHz), the wavelength of the electromagnetic field becomes comparable to the dimensions of the discharge

vessel used in microwave discharges, which necessitates special coupling mechanisms. Most microwave-induced plasmas are produced in a waveguide structure or resonant cavity. As the dimensions of the cavities diminish when the frequency increases, the maximum microwave frequencies used for discharge applications are usually below 3 GHz. A very common frequency is 2.45 GHz, which is also used in microwave ovens.

Since at these frequencies only the light electrons can follow the oscillations of the electric field, microwave plasmas are normally far from local thermodynamic equilibrium. They can be operated in a wide pressure range, starting from below 1 mbar to about atmospheric pressure. These discharges can produce large volume non-thermal plasmas of reasonable homogeneity. A typical microwave excimer lamp is composed of a power supply unit, a ventilation unit, and a lamp house containing two microwave generators and a discharge tube. The microwave power generated by two magnetrons is fed to a microwave cavity through waveguides and coupling antennas. The discharge tube is a sealed fused quartz containing excimer gas and air cooled during operation. Ametepe et. al reported conversion efficiencies from electrical power to optical power are from 20-40% [13]. Their high efficiency is due to gas cooling, which results in increasing the excimer intensity as a result of lower gas temperature.

Another configuration that can be used for excimer generation is the corona discharge. The electrodes in a corona discharge are simply a pin and a plane electrode. In this configuration the electric field is not uniform and is highest at the tip of the pin electrode. This nonuniform electric field leads to

locally confined ionization channels and excitation processes long before a complete breakdown between the electrodes occurs [14]. Although sometimes corona discharges are undesirable, such as in power lines and communication antennas, they are found to be useful in air purification devices and radiation detectors and counters. Most recently corona discharges were used for excimer generation in rare gas halide mixtures [7]. In this experiment, a needle grid electrode configuration was used to produce a positive corona discharge in a mixture of $He/Xe(Kr)/SF_6/CCl_4$, which is used for multiwavelength excimer radiation sources. The positive corona discharge results in the excitation of the atoms and formation of excimer molecules mainly through electron impact and harpoon reactions, respectively.

Microhollow cathode discharge (MHCD) is another type of gas discharge between two electrodes separated by a dielectric layer 200 μm thick and a hollow structure in the center with a diameter in the range of 100-200 μm. MHCDs have evolved from hollow cathode discharges, which were used for high power laser and opening switches, had an opening in the mm range, and are normally operated at low pressure (mTorr to Torr range). According to White's scaling law [15], the sustaining voltage scales with the product pD, where p is the gas pressure and D is the hole diameter. Keeping pD constant and decreasing the hole diameter, the gas pressure can be increased, which would be efficient for excimer formation. Different research groups have been studying MHCDs for excimer generation using rare gases and rare gas halides [Old Dominion University, Stevens Institute, University of Illinois, University of Erlangen-

Nuremberg]. DC MHCD has been established in xenon with an efficiency of 6-9% [3] at a low sustaining voltage of 200 V. Also it has been operated in argon, and it showed the possibility of operating multiple discharges in parallel, a concept which promises to be used as a flat excimer lamp [16].

The advantages of MHCDs are low cost, compact size, and low operating voltage. Although the obtained efficiency (6-9%) in xenon MHCD is lower than the theoretically calculated value of 30-40% [3], due to the high gas temperature, it is expected that by pulsing the discharge with short pulses (ns range), higher efficiency can be obtained. Also MHCDs have been obtained in Xe (172 nm), Ar (127 nm), and Ne (84 nm), which finds applications in semiconductor processing requiring short wavelength radiation for better resolution.

CHAPTER II

EXCIMER FORMATION AND DECAY

Excimers (excited dimers, trimers) are weakly bound excited states of molecules with a repulsive ground state [17]. Excimer lamps have a wide range of applications depending on their emission wavelength range, which depends on the gas used. Excimer gases are either rare gases such as Xe, Ar, Ne, and He or rare gas halides such as XeCl, ArF, KrF, and XeF. Figure (2.1) shows a chart of various excimer gases that have been used for excimer generation and the corresponding wavelength of each [18]. As can be seen, excimer emission from both rare gas and rare gas halides is in the UV and VUV range, and according to the required wavelength, a specific gas can be chosen.

Excimer formation requires mainly two conditions: a) high energy electrons, higher than the threshold energy for the excitation cross section, to excite the ground atoms, and b) high pressure, near atmospheric pressure, which makes the three-body collisions more favorable. Depending on the gas pressure range, excimer molecules will radiate either in the first continuum (low pressure), from high vibrational levels, or second continuum (high pressure), from low vibrational levels, as shown in figure (2.2) [19]. At very low pressures, excimer formation is less likely, and therefore, resonant line emission occurs when excited atoms emit spontaneously to the ground level. Figure (2.2) shows an energy level diagram of an excimer gas with the different possible emissions. The wavelength of the resonance line and excimer continua is shown in table (2.1).
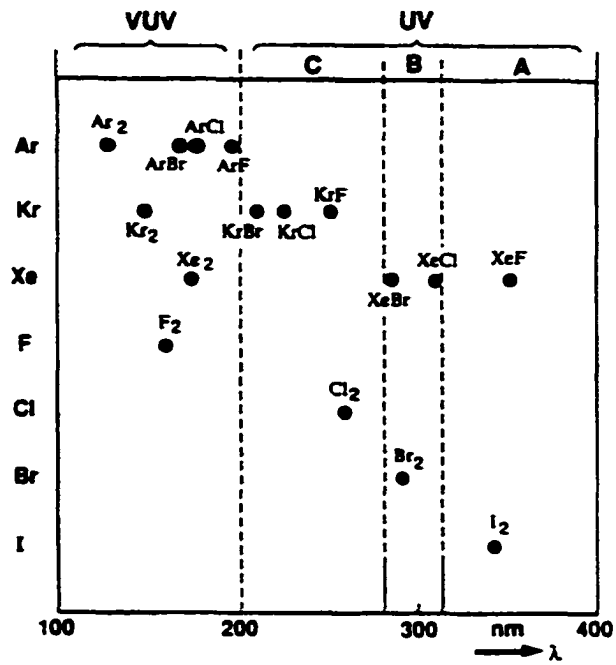
Figure (2.1) A chart of different excimer gases used in excimer lamps as a function of radiation wavelength [18].
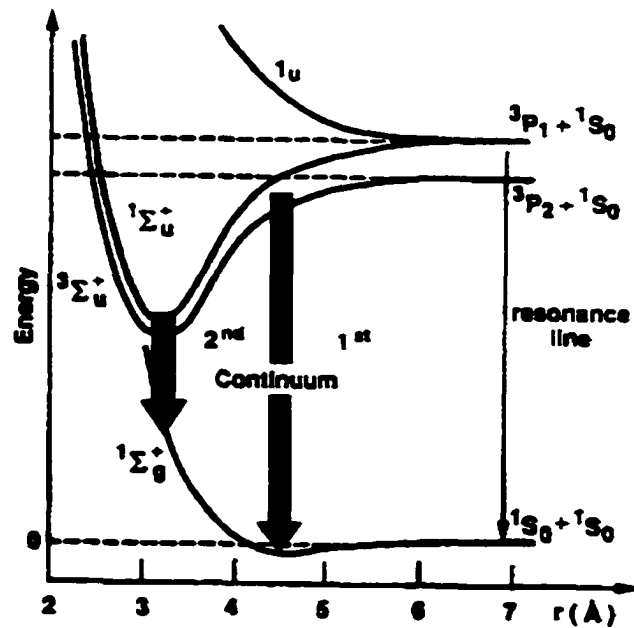
Figure (2.2) A typical energy level diagram for an excimer gas [19].

Table (2.1) Resonance line and excimer continua radiation for Ar and Xe:

Rare Gas	Resonance Line	1st Continuum	2nd Continuum
Argon	106.4	110 nm	127 nm
Xenon	146.96	150 nm	172 nm

Excimer formation requires both high-energy electrons and high pressure, so three-body collisions will be more favorable. Excimer kinetics can be divided into three major processes: a) atoms excitation, which is the precursor for excimers; b) excimer formation; and c) excimer decay. The physics of these processes have been studied extensively to understand their main controlling parameters [17,20-22]. The high-energy electrons are obtained either from a high-energy electron beam, or by accelerating the secondary electrons in the cathode fall area as in MHCDs. Figure (2.3) shows the energy level diagram for a rare gas and the possible reaction that could take place [17]. Excimer formation can be described as due to excitation of the gas atoms by high-energy electrons to the metastable state (^{3}P):

$$e + X \rightarrow X^* + e \tag{2.1}$$

where X is the rare gas atom and X* is the excited metastable atom. The excited atom can decay emitting the resonance line or go through a three-body collision according to:

$$X^* + X + X \rightarrow X_2^* + X \tag{2.2}$$

where X_2^* is the excimer molecule. This reaction is more favorable at high pressures, and the excimer molecules decompose giving their excitation energy in the form of UV or VUV photons according to:

$$X_2^* \rightarrow 2X + h\nu \qquad (2.3)$$

where $h\nu$ is the excimer radiation. These reactions in addition to other transitions that could take place in excimer formation are shown schematically in figure (2.3) [17].

One of the first kinetic models for rare gas excimers was presented by Lorents [20] and was later modified by Werner et. al [21]. In this model, the mechanism for selectively populating the excimer levels can be viewed as a sequence of collisional energy exchange. In the following sections, a model based on different works [17,20,21,23] in excimer formation is discussed.

2.1 Excimer Precursors

As mentioned earlier, high-energy electrons can be generated either through a gas discharge or using an electron beam. These electrons, when colliding with the gas atoms, result in either excitation or ionization depending on the electron energy.

$$X + e \rightarrow X^+ + 2e \qquad (2.4)$$

$$X + e \rightarrow X^* + e \qquad (2.5)$$

$$X + e \rightarrow X^{**} + e \qquad (2.6)$$
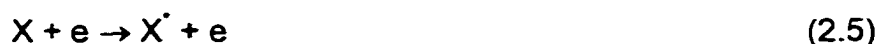
where X^+ is the rare gas ion, X^* is the rare gas excited states ($^3P_1$ & $^3P_2$), and X^{**} is the higher lying states. Exciting the gas atoms is the first step in excimer formation as can be seen from equation (2.1). Also according to this model, X^{**}

MOLECULAR   ATOMIC
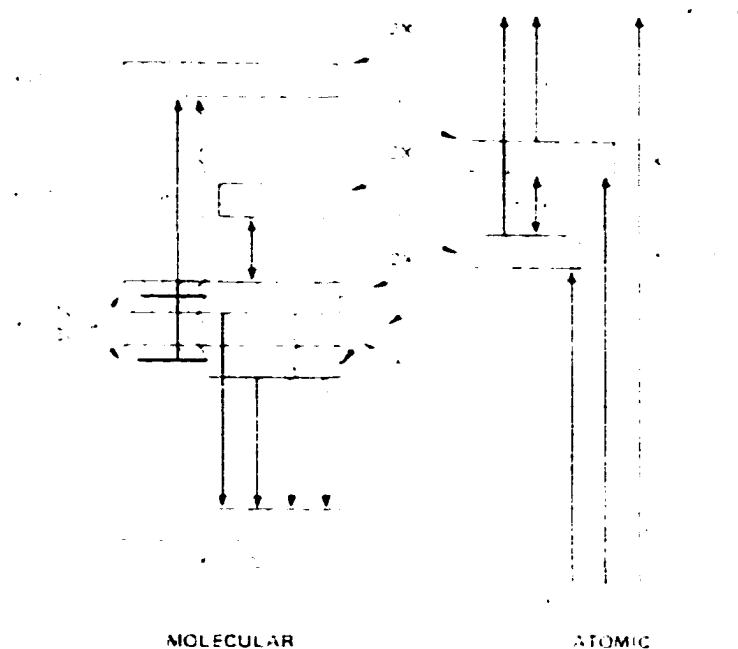
Figure (2.3) Schematic diagram of the possible reaction that could take place in the process of excimer formation. The gas atoms (X) can be either excited (X*) or ionized (X⁺) by the electrons (e). At high pressure the excited atoms goes through a three-body collision forming the excimers (X₂*) at $^1\Sigma$ and $^3\Sigma$ states. These excimers decompose while decaying and produce their energy in the form of UV or VUV photons [17].

and X^+ are partly responsible for populating the X^* state.

Collisional radiative recombination is the main loss mechanism for the X^+ atomic ion at low pressure; while at high pressure, it is through the formation of a diatomic molecular ion through three body collision:

$$X^+ + X + X \rightarrow X_2^+ + X \qquad (2.7)$$

This diatomic ion either will capture an electron followed by dissociation to the ground state (dissociative recombination):

$$X_2^+ + e \rightarrow X + X^{**} \qquad (2.8)$$

or it will involve in cluster ion formation through three-body collision and then be lost by dissociative recombination as in equation (2.8):

$$X_2^+ + X + X \rightarrow X_3^+ + X \qquad (2.9)$$

As for the X^{**} atoms, it relaxes via the reactions

$$X^{**} + 2X \rightarrow X_2^{**} + X \qquad (2.10)$$

$$X_2^{**} + (X) \rightarrow X^* + X + (X) \qquad (2.11)$$

2.2 Excimer Formation

Excimer formation is achieved via three-body collision with the excited gas atom X^* according to:

$$X(^3P_1) + 2X \rightarrow X_2^*\left(^1\Sigma_u v \gg 0\right) + X \qquad (2.12)$$

$$X(^3P_2) + 2X \rightarrow X_2^*\left(^3\Sigma_u v \gg 0\right) + X \qquad (2.13)$$
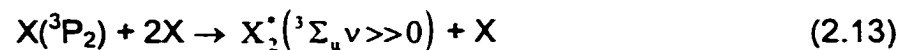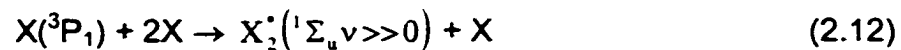
Depending on the vibrational relaxation, low or high, the molecules will emit from the high or low vibrational levels corresponding to a 1st or 2nd continuum excimer emission, respectively:

$$X_2^*\left(^1\Sigma_u v >> 0\right) + X \rightarrow X_2^*\left(^1\Sigma_u v \approx 0\right) + X \qquad (2.13)$$

$$X_2^*\left(^3\Sigma_u v >> 0\right) + X \rightarrow X_2^*\left(^3\Sigma_u v \approx 0\right) + X \qquad (2.14)$$

$$X_2^*\left(^1\Sigma_u v >> 0\right) \rightarrow 2X + h\nu_1 \qquad (2.15)$$
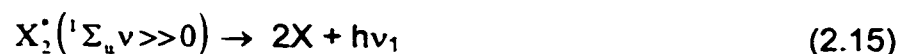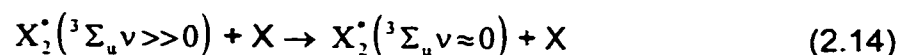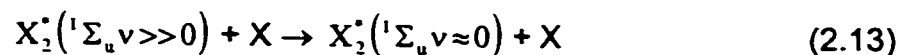
where $h\nu_1$ is the first continuum radiation energy or:

$$X_2^*\left(^1\Sigma_u v \approx 0\right) \rightarrow 2X + h\nu_2 \qquad (2.16)$$

where $h\nu_2$ is the second continuum radiation energy.

2.3 Excimer Decay Mechanism and Loss Processes

A summary of the radiative lifetimes for various rare gases have been tabulated by Lorents [20] of which Xe and Ar lifetimes are listed in table 2.2.

Table 2.2 Radiative lifetime of Ar_2 and Xe_2:

Excimer molecule	$^3\Sigma_u$ (µs)	Ref.
Ar_2^*	2.8	25
	3.7	26
	3.2 ± 0.3	27
	4.0 ± 2.0	24
	3.22	28
Xe_2^*	0.09 ± 0.05	27
	0.10 ± 0.05	24
	0.140 ± 0.045	24

In the presence of hot plasma electrons, both the excimer states and their precursors will go through reactions of the type:

$$e + X_2^*(^3\Sigma) \rightarrow e + X_2^*(^1\Sigma) \qquad (2.17)$$

At high electron densities super elastic electron collisions can enhance electronic relaxation in both the atomic and excimer manifolds. However, superelastic collisions can destroy excimers by causing transitions to the ground state:

$$X_2^* + e \rightarrow 2X + e \qquad (2.18)$$

The excited excimer species may also participate in a destructive process of the form:

$$X_2^* + X_2^* \rightarrow X_2^+ + 2X + e \qquad (2.19)$$

which is refered to as Penning ionization. The Penning process represents a significant loss mechanism at high excimer densities. An additional loss process that plays an important role specially with increasing temperature is the quenching of excimers by neutral atoms:

$$X_2^* + X \rightarrow X^* + 2X \qquad (2.20)$$

A complete list of the kinetic processes in xenon with the rates of different reactions is given in table A.1 [29].

CHAPTER III

MICROHOLLOW CATHODE DISCHARGES

3.1 Hollow Cathode Discharges

Hollow cathode discharges are gas discharges between two electrodes where the plane cathode in plane electrodes glow discharge is replaced by a cathode with a hollow structure, and for a certain range of operating conditions, current and pressure, the negative glow is inside the hollow structure of the cathode [30]. Different geometric configurations such as cylinderical, spherical, slit, or helical have been presented for hollow cathode glow discharge as shown in figure (3.1) [30]. The voltage in hollow cathode discharges is found to be lower than that of plane electrodes at a constant current, and the current is orders of magnitude higher, corresponding to a much higher current denisty, at a constant voltage. This is refered to as hollow cathode effect. Measurements by White showed that the plasma in the hollow structure contains up to 1 eV electrons in concentrations greater than 10^{13} /cm^3 [15].

Schaefer and Schoenbach have listed different mechanisms that might contribute to the hollow cathode effect [30]. One of these mechanisms is pendel electrons, where the electrons emitted from the cathode surface by secondary electron emission are accelerated in the cathode fall and result in increasing the excitation and inoization rates in the negative glow region. Electrons that didn't suffer from high energy loss in the negative glow are reflected back by the opposite cathode surface to the negative glow, which enhances the excitation process. This effect influences the electron energy distribution function (EEDF)
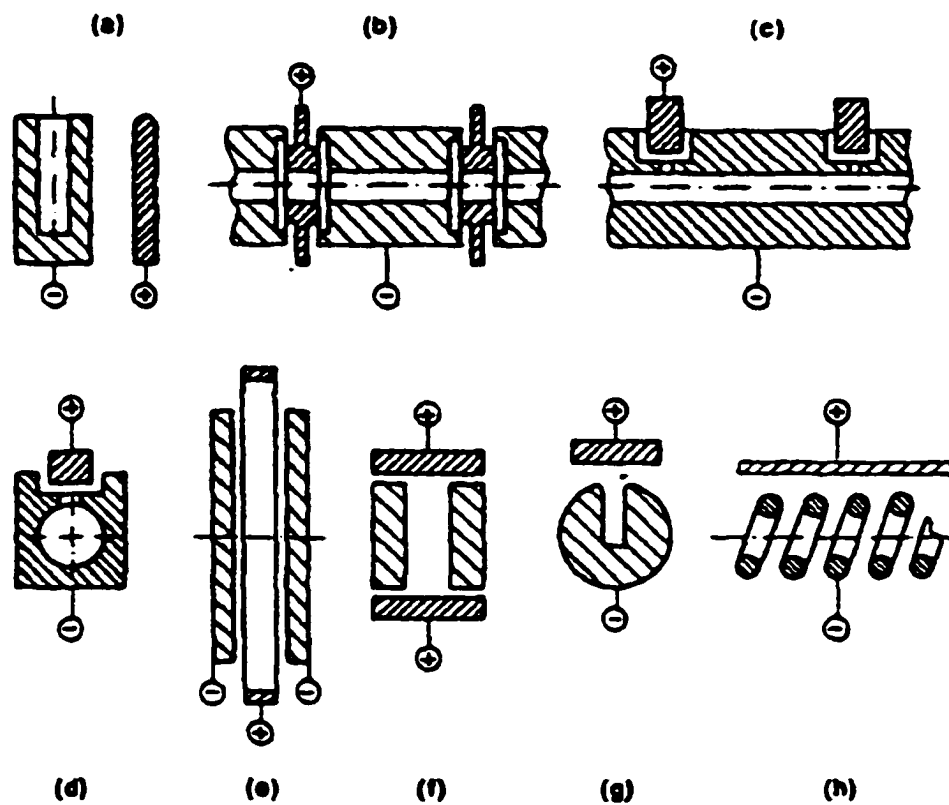
Figure (3.1) Typical holllow cathode geometries a), b), c) cylinderical; d) spherical; e) parallel plate; g) slit; and h) hellical [30].

in hollow cathode plasma as was measured by Gill and Webb [31]. They found that the EEDF close to the negative glow/dark space boundary has a non-maxwellian distribution with a high energy tail with energies higher than 100 eV as shown in figure (3.2) [31]. Similar to plane electrodes configuration, a threshold voltage has to be applied before breakdown. An expression for the breakdown voltage was derived by Eichron et. al for a one-dimensional hollow cathode discharge model [32]. A two-dimensional hybrid model of glow discharge in hollow cathode configuration showed similar V-I characteristics to plane electrodes at low current, Townsend discharge, as shown in figure (3.3) [33]. As the curent increases, a negative resistive behavior is observed coresponding to the the hollow cathode effect.

3.1.1 Lower limit of the Hollow Cathode Discharge

The lower limit in pressure for the hollow cathode effect is determined by the loss of pendel electrons, which reach the opposite cathode wall and are removed from the discharge. This condition leads to an expression for the minimum value of pD at which the hollow cathode discharge can be sustained [34]:

$$pD = \ln f^{-1} \Big/ \left(\langle \sigma \rangle n_0 \right) \qquad (3.1)$$

where n_0 is the gas density at a pressure of 1 Torr, f is a loss factor, and $\langle \sigma \rangle$ is the average collision cross section. It was found that for Argon the critical value for pD is 0.026 Torr cm.
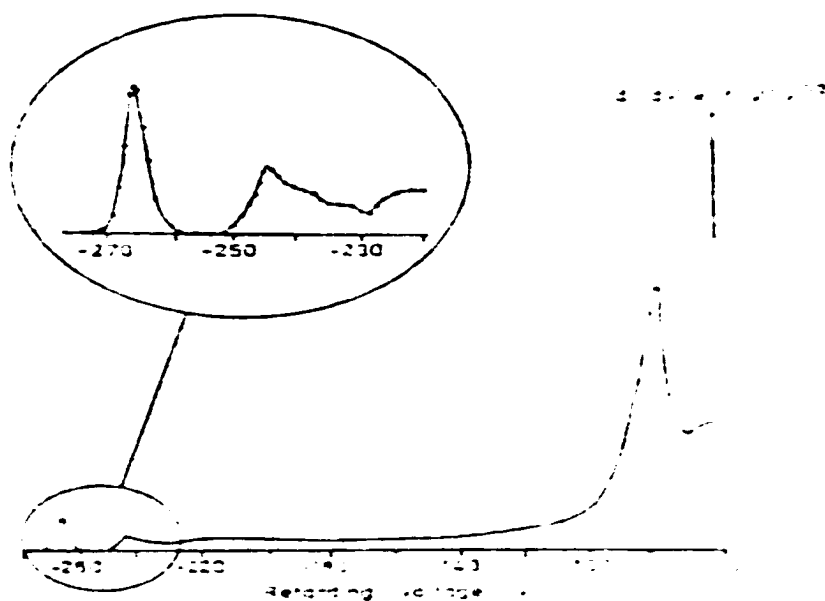
Figure (3.2) Electron energy distribution function close to the negative glow/cathode dark space boundary showing the cathode fall beam component and the first collision structure in details [31].

3.1.2 Upper Limit of the Hollow Cathode Discharge

The upper limit for pD was found to be approximately 5 Torr cm in experimental studies performed in PERI laboratory [34], and a model describing the upper limit in pressure for hollow cathode discharge operation was presented. Increasing the current in hollow cathode discharge switches the discharge to an abnormal glow discharge, where increasing the current is obtained by increasing the cathode fall voltage and the slope of the current-voltage characteristic turns positive again. The pD value for the transition from the hollow cathode discharge to the abnormal glow discharge can be estimated by assuming that the pendulum motion of the electrons ceases to exist when the sum of the lengths of the two opposite cathode falls and the negative glow becomes smaller than the cathode hole diameter. The cathode fall thickness for plane cathodes is given by [35]:

$$d_{an} = B*/p + B/J^{1/2} \qquad (3.2)$$

where B* and B are constants depending on the gas and electrode material, and J is the current density. The negative glow length for argon discharge and a potential drop of 200 V is l_0 = 1 cm at a pressure of p_0 =1 Torr [36]. Assuming that this distance scales linearly with 1/p, then the condition for the upper limit in pD for hollow cathode discharges is:

$$pD = 2B* + 2pB/J^{1/2} + l_0 p_0 \qquad (3.3)$$

For argon (and an aluminum cathode), B* is 0.054 Torr.cm and B is 0.0034 cm.A$^{1/2}$ [35]. This upper limit was found to be much smaller than the experimentally obtained value of 5 Torr cm [34].
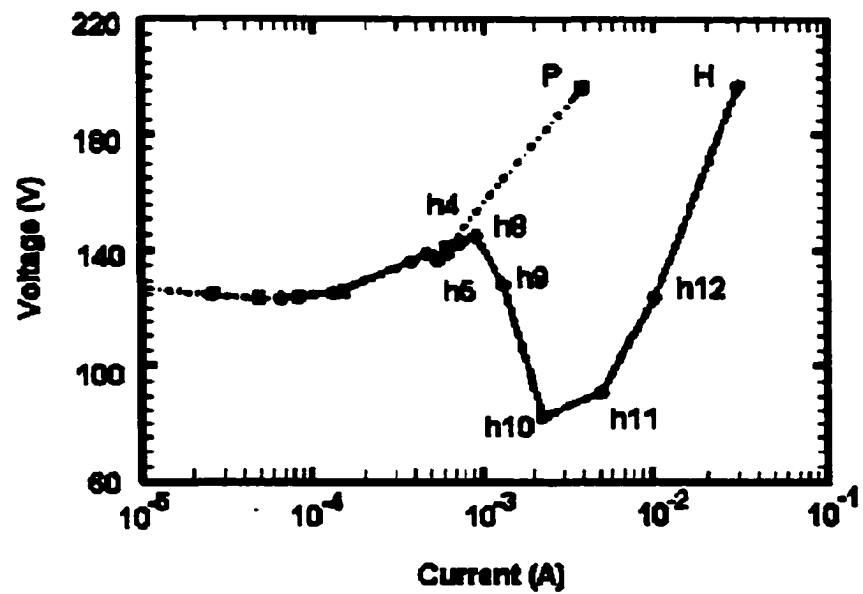
Figure (3.3) Voltage-current characteristics for hollow cathode (solid line) and plane cathode (dashed line) geometries. At low current h1-h4 it is a Townsend discharge. With increasing current hollow cathode and then normal glow discharge up to h11. With further increase in the current, it switches to abnormal glow discharge [33].

3.2 Microhollow Cathode Discharges (MHCDs)

According to White's scaling law [15], the sustaining voltage of the discharge is scaling with pD and I/p as:

$$V = V(pD, I/p) \qquad (3.4)$$

where V is the sustaining voltage and I is the discharge current. In his experiments, White has found that by keeping the pD product constant, higher pressure operation can be achieved by decreasing the hole diameter and the discharge showing similar characteristics. Hollow cathode discharges with smaller diameters in the range of hundreds of micrometers are referred to as "Microhollow Cathode Discharge" (MHCD). According to the experimentally obtained pD upper limit of operation of hollow cathode discharge of 5 Torr cm [34], decreasing the cathode hole diameter to 100-200 µm would allow to increase the operating pressure. Microhollow cathode discharges are direct current, high-pressure gas discharges between perforated electrodes, separated by thin layers of dielectric with thickness in the range of 100-250 µm and a hole diameter ranging from 100 to 200 µm. Different groups [3-6,16,39-45] have studied the characteristics of MHCDs in rare gases, rare gas halides as a VUV excimer source, and the possibility of operating arrays of MHCDs in parallel. Parallel operation of MHCDs at high pressure (several hundred Torrs) has been achieved by using single ballast (silicon layer) as the anode [39,42,43].

In DC operation of MHCD in xenon, the internal efficiency of excimer emission at 172 nm (output VUV optical power to input electrical power) was measured to be in the range of 6-9% [38]. The spectral measurements showed

an increasing VUV radiation at 172 nm with increasing pressure and peaking at a pressure of 400 Torr, as can be seen in figure (3.4) [38]. The increasing intensity with pressure is due to the increasing three-body collision reactions and, hence, excimer formation. It was expected that the intensity would keep increasing with increasing pressure, but it peaked at 400 Torr and decayed. This is assumed to be mainly due to the increasing gas temperature, which would result in increasing the quenching processes and the loss of excimers. An I-V characteristic of MHCD was measured and showed a resistive behavior at low currents followed by a negative resistance effect (hollow cathode effect). The DC current was limited to 8 mA to avoid thermal damage of the electrodes. Measurements of the output VUV optical power showed a linear dependence on current.

Excimer emission from MHCDs in noble gases is constrained inside the hole, as long as the upper limit of pD is not exceeded, as a result of the pendel electrons. But VUV images of MHCD have shown the excimer emission to be both inside the hole and expanding on the cathode surface with increasing current as will be shown later. Since the pendel effect can't be applied outside the hole there must be other mechanisms involved in the process. Another possibility for coupling in MHCDs is through excimer photons. In this case, photons would travel across the gap and secondary electrons will emit from the cathode surface when photons reach the cathode. In case of instability, at one side of the cathode hole, the gas temperature would increase and as a result, the excimer emission at this point would decrease along with the number of photons.

With a lower number of photons the number of secondary electrons due to photon collision will decrease. The electron density also decreases producing a negative feedback. This model would be valid if the discharge was constrained in the hole, which is not the case, since the possibility of photons colliding with the cathode surface outside the hole is lower than inside. Photons would just go through the discharge, and hence, coupling through photons is less probable.
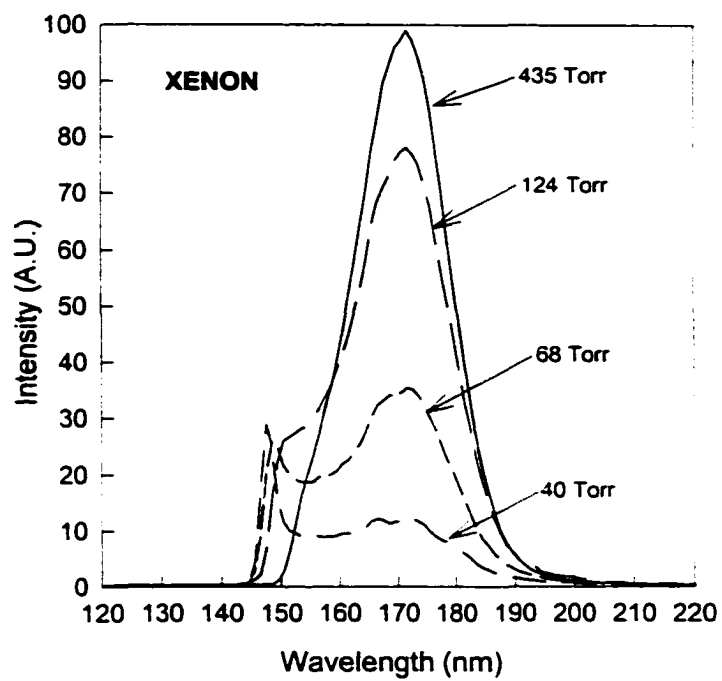
Fig. (3.4) Pressure dependence of the VUV emission spectrum of high pressure MHCD in xenon [4].

CHAPTER IV

Experimental setup

4.1 Sample Configuration and Construction

A MHCD uses two electrodes separated by a dielectric layer with a thickness of 250 μm and a hole in the center with a diameter in the range of 100-200 μm [4]. Molybdenum was used as the electrode material due to its high melting temperature of 2896 K. In these experiments circularly shaped electrodes 100 μm thick and 1.6 cm in diameter were used. Two different dielectric spacers were used, mica or alumina, with a thickness of 250 μm. The three layers (two electrodes and a dielectric) were stacked using either a 5-minute epoxy glue or a two components silver epoxy (hardener and silver epoxy) from Epoxy Technology. Silver epoxy was used in most of the experiments since its thermal characteristics allow working at higher temperatures compared to the 5-min epoxy which when used would result in contaminating the discharge chamber and would lowered the excimer radiation efficiency. A certain procedure was followed in preparing the sample. After cutting the disc electrode they are polished and cleaned with acetone in order to get rid of any deposits that might have been on the surface. Stacking the electrodes to the dielectric is achieved by applying a well-mixed one to one ratio of the two components of the epoxy glue between the discs and the dielectric near the edges away from the center. The next step is curing the epoxy by placing the sample in a high temperature oven of about 180 °C for at least 30 minutes.

The hole of MHCD samples can be achieved either by mechanical or laser drilling. For samples with mica as a dielectric mechanical, drilling was used. Due to the hardness of alumina, mechanical drilling was not possible, and a KrF excimer laser radiating at 248 nm was used. The laser settings used for drilling are adjusted to a pulse energy of 22.9 mJ with a repetition rate of 100 Hz and a total number of 2,000 pulses. According to the best focusing that could be maintained, the resulting hole had a conical shape rather than cylindrical with a diameter ratio of 2/3 as is shown schematically in figure (4.1).

4.2 Electrical Circuit

4.2.1 DC Operation

MHCDs can be operated either in DC or pulsed. The DC circuit consists of the high voltage power supply and a 100 kΩ current limiting resistance (R_{clr}), to avoid damaging the sample during breakdown due to high current, and a 1 kΩ current viewing resistance (R_{cvr}) [34]. Figure (4.2) shows the electrical circuit used for DC operation [34]. Both discharge voltage and the voltage across the current viewing resistance (proportional to the current) were measured using a digital multimeter.

4.2.2 Pulsed Operation

There are two possible modes of pulsed operation. They can be characterized with respect to the characteristic time constants at overvolted conditions (discharge conditions where the applied voltage exceeds the sustaining voltage). These include the time constant for glow-to-arc transition, τ_{ga}, and the time constant for melting the electrodes caused by the high current

Figure (4.1) Typical MHCD sample

$R_L = 100 \, k\Omega$
$R_A = 1 \, k\Omega$
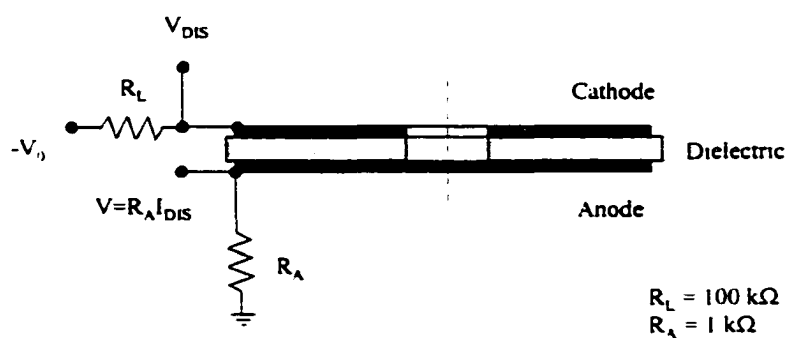
Figure (4.2) DC electrical circuit [34]

densities in microhollow cathode discharges at high overvoltage, τ_e. The values of these time constants are dependent on gas, over voltage, pressure, and cathode material. One of the main causes of glow-to-arc transition is a thermal instability, which is associated with change in gas density, N, due to heating the neutral components [46]. In an atmospheric pressure gas discharge in argon, the time constant of glow-to-arc transition was found to be in the range of 36 ns, as will be discussed in detail in chapter VI. The time constant for melting the electrodes at high current, τ_e, is on the order of milliseconds.

The discharge can be operated using pulses with pulse rise and pulse duration longer than τ_{ga} but short compared to the time for thermal damage of electrodes, τ_e. This operation will be referred to as equilibrium pulsed operation [47]. Pulsing the discharge in this mode allows us to avoid the thermal loading and consequently to reach higher currents than in DC operation. In this case, the excimer emission is based on the same processes (electrons have the same energy distribution) as for DC operation. Using these long pulses, the transient temporal development of the excimer radiation during breakdown and discharge decay was explored.

Pulses with pulse risetime and short duration compared to any of the two time constants require nanosecond pulsing. In this mode, the electron energy distribution is shifted towards higher values and will be referred to as non-equilibrium pulsed operation. Experiments in atmospheric pressure air [48] had indicated that extremely short pulses could affect the electron kinetics without heating the plasma. The pulsed electric field shifts the electron energy

.

distribution to higher values and consequently causes a nonlinear increase in the excitation and ionization rates and would convert into an increase in efficiency. Investigation of the response of MHCD to transient voltages allows for the measurements of relaxation time of electrons and radiation. Also better understanding of these phenomena allows optimization of excimer emission and provides data on particle kinetics.

4.2.2.1 Pulse Generator for Equilibrium Pulsed Operation

In equilibrium pulsed operation, a semiconductor pulser was built using a metal-oxide-semiconductor field-effect-transistor (MOSFET) as a switch. Figure (4.3) shows a schematic diagram of the circuit used for this mode of pulsed operation. The circuit can be divided to three main parts: trigger, driver, and switch. The driver is used to supply current to the gate of the MOSFET, which allows fast switching, and consists of two stages of Bipolar Junction Transistors (BJTs). A Stanford Research pulse generator model DG535 that supplies a controlled pulse repetition rate and width with amplitude of 4 V was used to trigger the driver. The third part of the circuit is the switching using an IGBT MOSFET model IXBH 40N160. The characteristics of this power MOSFET allows up to 1600 V output voltage with up to 33 A [49]. The switching time is in the range of 200-300 ns, which does not affect the performance for equilibrium pulsed operation. When the pulse is applied to the sample, the voltage increases up to the breakdown voltage and then drops to the sustaining voltage of the discharge of about 200-230 V as shown in figure (4.4). For time resolved measurements in pulsed operation, a Tektronix digital oscilloscope model TDS
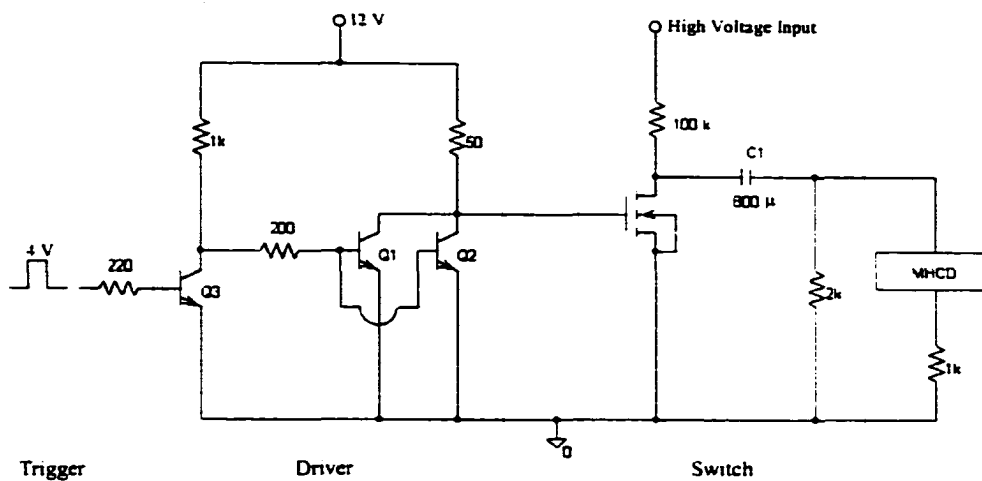
Figure (4.3) Schematic diagram of pulse generator used in equilibrium pulsed operation. The pulse width and duration is controlled by the trigger signal.
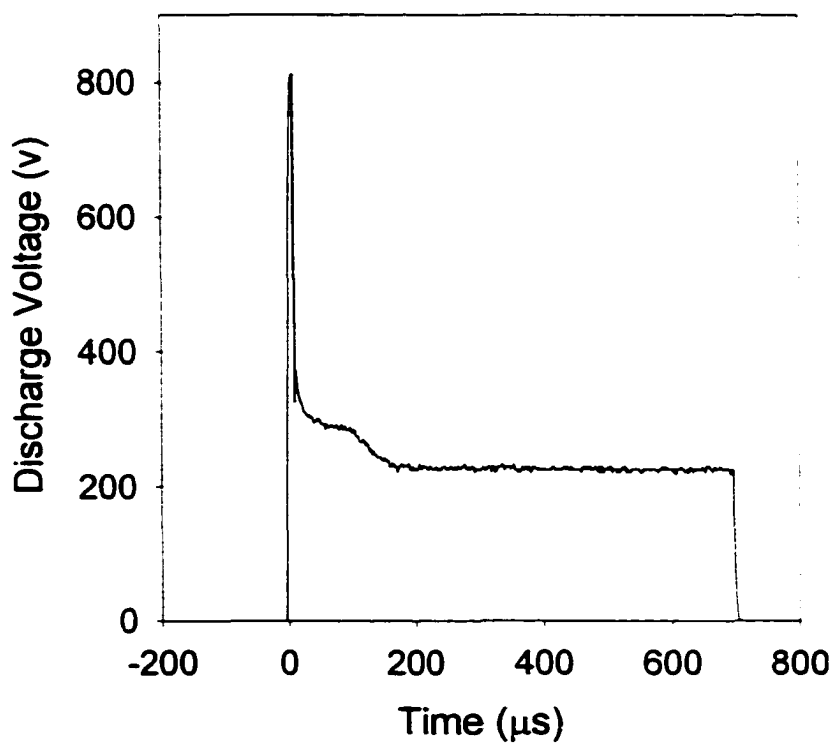
Figure (4.4) A typical voltage transient for MHCD in xenon. The voltage increases till it reaches the breakdown voltage where V drops to the sustaining voltage.

3054 was used. The voltage was measured using a voltage probe (TEK5100) with a maximum voltage of 2500 V and a 250 MHz bandwidth.

4.2.2.2 Pulse Generator for Non-Equilibrium Pulsed Operation

In this mode of operation, a Pulse Forming Network (PFN) was used in combination with a semiconductor switch. The pulse generator is similar in design to a system described in [50]. The main advantage of this PFN over using a MOSFET in an on and off mode is that it would provide a faster rise and decay time. This would allow for shorter pulses, and changing the cable length changes the pulse width. The PFN used in this experiment is a Blumlein circuit [51] that uses a coaxial cable (RG58) as an energy storage medium until it discharges in the load when the MOSFET is switched on. Figure (4.5) shows a schematic diagram of a typical Blumlein pulser where the coaxial cable builds up voltage until the switch turns on and discharges in the 50 Ω matching load. In "ns" pulsed operation, the short pulses were superimposed to a DC discharge, which was archived in the circuit shown in figure (4.6). The diode serves as a buffer between the two circuits, so the 50 Ω matching resistance wouldn't be seen by the DC circuit, which would prevent breakdown of the discharge. The pulse generator design in "ns" pulsed operation uses an n-channel enhancement MOSFET model DE275-102N06A (IXYS). The advantage of this MOSFET is its fast switching time in the range of 3-4 ns, which allows for short pulses in the 10 ns range [49]. A typical voltage pulse is shown in figure (4.7) for different cable lengths.
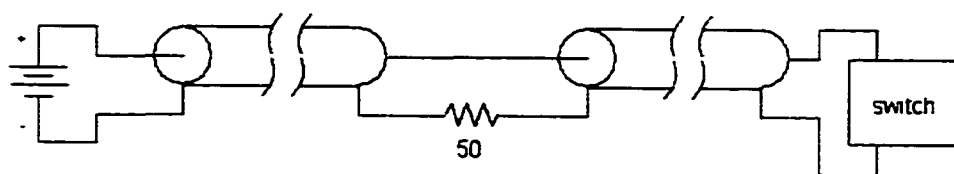
Figure (4.5) Schematic diagram of a typical Blumlein circuit.
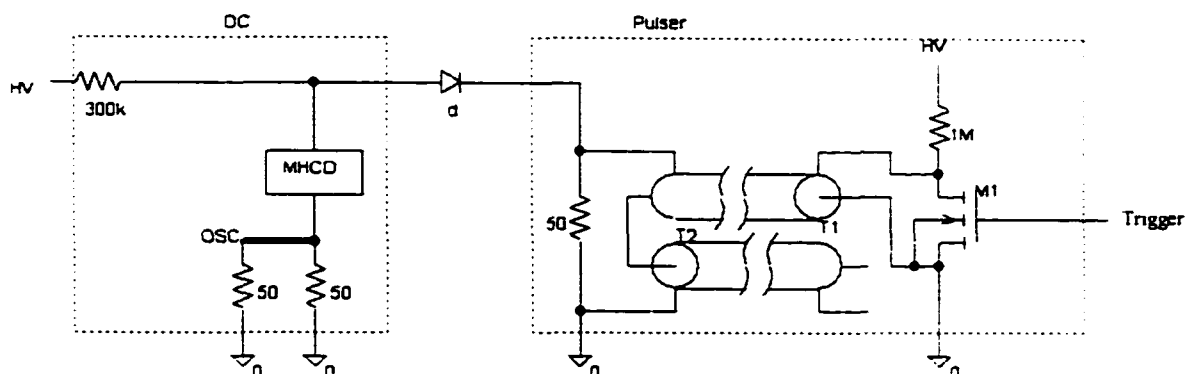
Figure (4.6) Schematic diagram of the electrical circuit used for short pulse operation.
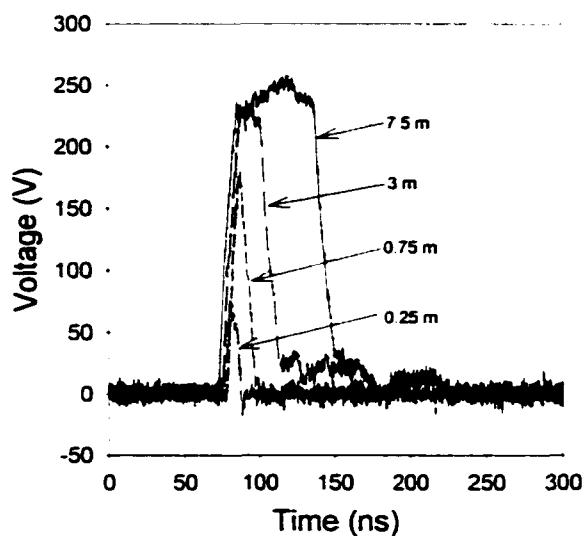
Figure (4.7) ns voltage pulse with various pulse widths determined by the cable length.

4.3 Discharge Cell

The sample is placed in a stainless steel chamber and held with a macor holder with two copper rings for electrical connections. The chamber is connected to a turbo molecular pump that allows a vacuum down to 10^{-6} Torr. Due to the wavelength range that is being studied (UV and VUV), special windows with high transmittance must be used. The windows used are either MgF_2 or LiF due to their high transmittance of 80-95 % at this wavelength range of 172 nm and 127 nm.

Two gases have been studied for VUV excimer generation in MHCDs, xenon (Xe) and argon (Ar). MHCD in xenon were operated in a static gas due to the high cost of high purity xenon (99.997%). In the case of argon discharges static operation resulted in a low efficiency, and many impurity lines were observed such as oxygen, nitrogen, and carbon. To overcome this problem, MHCDs in argon were operated in a flowing gas, and the flow rate was controlled by a mass flow meter controller model MFC8160 (coastal instruments). Figure (4.8) shows a schematic diagram of the discharge cell used.

4.4 Spectral Measurements

Different measurements have to be performed to measure an absolute value of the output optical power and can be categorized as arbitrary units spectral measurement, calibrated detector measurements, and correction for the spectral response of the used components.

4.4.1 Spectrometer Setup

Two monochromators have been used for spectral measurements, the 0.2 m and 0.5 m McPherson monochromator. For measurements of VUV excimer radiation in both xenon (172 nm) and argon (127 nm), a 0.2 m vacuum VUV McPherson monochromator (model 234/302) was used. This monochromator covers a spectral range from 50 nm to 300 nm and contains a concave holographic grating with a groove density of 1200 G/mm and is blazed at 150 nm [52]. The scanning can be controlled either manually or using a scanning controller model (789A-3) to control a stepper motor that controls the positioning of the grating. Figure (4.9) shows a schematic diagram of the monochromator setup. Since the monochromator is being used for VUV radiation measurements, it is connected to an ALCATEL DRYTEL 31 pump. For high spectral resolution, the slit widths (both entrance and exit) were adjusted to 100 μm. The light was collected using a detector assembly consisting of a sodium salicylate scintillator and a Hamamatsu photomultiplier tube (PMT) model R1533 that covers a wide spectral range from 30 to 600 nm [53]. The PMT power supply is a Hamamatsu model C3830 and the voltage applied to the PMT ranged between 800 V to 1200 V according to the intensity of the detected signal. A program written to control the stepper motor and collect the data from the PMT after converting it using an analog to digital converter was used to collect the output of the PMT.
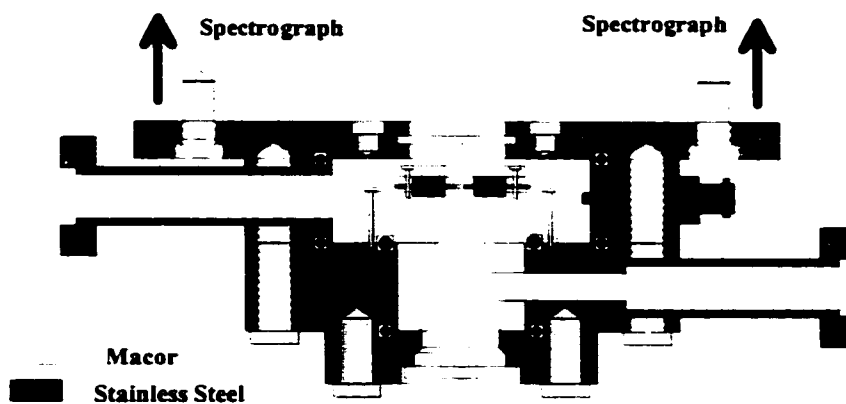
Figure (4.8) Schematic diagram of the chamber used for the MHCD experiments.
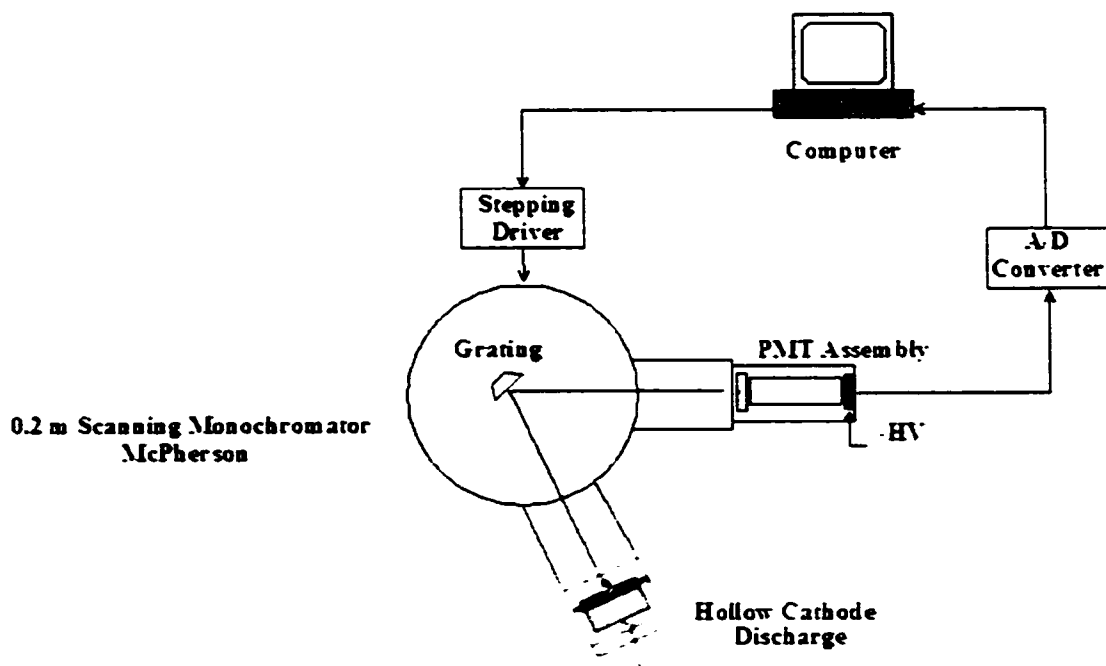
Figure (4.9) 0.2 m VUV monochromator experimental setup.

4.4.2 Electron Density Measurements

Electron density is an important factor in determining the efficiency of excimer formation. Thomson scattering, interferometry, and line broadening are examples of the techniques used for electron density measurements. Line broadening could be natural since the quantum states of an atom don't have a single energy but a small spread in energy. Another type of broadening is the Doppler broadening by thermal particle motion and is proportional to $T^{1/2}$, where T is the gas temperature. A third cause for line broadening is pressure or collisional broadening, which is sometimes referred to as Stark broadening. Stark broadening arises from the influence of nearby particles upon the emitting atom. A quasistatic approach assumes the atom to radiate in an environment that is effectively static during the period of emission. Any individual radiator experiences a shift in the wavelength, and the average over all shifts gives the line width and shape. The shift in the spectral line due to electric fields is called the Stark shift.

In order to calculate the line shape in the quasistatic approximation, the relation between the line frequency and the electric field have to be known. In the case of hydrogen, the Stark effect is linear, while for other atoms it is quadratic and is much smaller. Also in hydrogen, the Stark effect causes a symmetrical spread of initially degenerate lines, which causes no net shift of the line, while in other atoms, shifts as well as broadening of the lines occur. The electric field that results in this line broadening is a microfield due to the neighboring ions in the plasma. The Stark width for H_α (656.2 nm) is significantly narrower than for H_β

(486.1 nm) and that is why the broadening of the H_β line was used for electron density measurements [54].

For electron density measurements, a 0.5 m McPherson monochromator model 219 is used. The grating is blazed at 250-600 nm with a groove density of 2400 G/mm. In this case, the spectra was collected using an ICCD-MAX camera system described in details later in this chapter. A schematic diagram of the 0.5 m monochromator is shown in figure (4.10). Since wavelength calibration is critical for electron density measurements using the Stark effect, the ICCD camera was calibrated using a mercury line at 435.8 nm. The spectrum of the mercury line was recorded with the monochromator center wavelength being set at 435 nm. The center wavelength of the monochromator is changed and both the wavelength interval and the number of pixels representing the change of the mercury line position in the spectrum are recorded. Knowing the wavelength interval and the corresponding number of pixels allows us to calibrate the wavelength. For the above-mentioned setup, a 1 nm range is represented by 67 pixels, and hence, the pixel size is 0.0149 nm. The ICCD camera has 512x512 pixels, and so it covers a wavelength range of 7.6 nm.

4.4.3 Calibrated Detector Measurements

Two different calibrated detectors have been used for absolute power measurements: a calibrated radiometer (IL1400) with a calibrated detector (SED185) and photodiode (SXUV-100). The radiometer has an 8 mm diameter photocathode with a quartz window. The photocathode responsivity covers the range between 160-240 nm peaking at 185 nm, which is most suitable for xenon
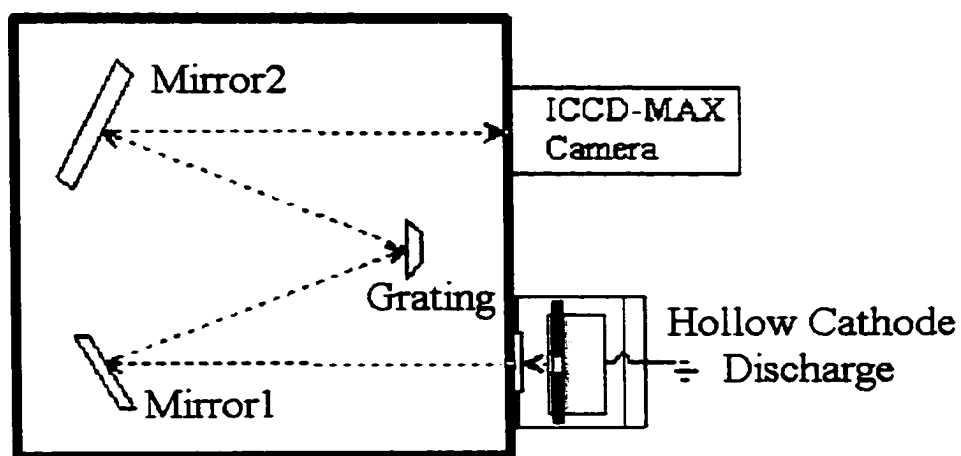
0.5 m Scanning Monochromator
McPherson (219)

Figure (4.10) 0.5 m McPherson monochromator experimental setup.

discharge (172 nm). The detector was placed in front of the discharge chamber at a distance of 1.9 cm with an air gap separation of 9 mm between the detector and the chamber window. The radiometer reading is given in W/cm^2 unit, and by assuming a point source radiation from the discharge and multiplying by $4\pi^2$ in addition to taking the responsivity of the detector, oxygen absorption, and the transmittance of the window into consideration, an absolute value of the total emitted power can be calculated.

In the case of argon discharge, a calibrated photodiode (model SXUV-100) supplied by IRD was used. The diode is a 1x1 cm^2 square area and covers a spectral range from 50 nm to 250 nm [55]. The diode was placed in the discharge chamber at a distance of 1.6 cm from the discharge with an optical filter in between. The transmission of the optical filter peaks at 125 nm and has a FWHM of 14.5 nm [56]. The output of the photodiode is measured using a KEITHLY 617 programmable electrometer giving the output in ampere units. Using the responsivity curve provided by the company, filter transmittance, and assuming a point source radiation in 4π solid angle, the total power can be calculated.

4.4.4 Pulsed Measurements

Both the radiometer and the photodiode are suitable for DC operation but can't be used for pulsed operation. In "ms" pulsed mode, a different setup shown in figure (4.11) was used to measure the output optical power. This system consists of a one to one imaging system, optical filter, and a PMT detector assembly. The absolute measurements of the DC operation were used to

calibrate the pulsed measurements. As for "ns" pulsed operation, the discharge was connected to the 0.2 m monochromator, and a time resolved output power was measured in the required wavelength range.

4.5 VUV Imaging

In addition to the electrical and spectral studies of the discharge, spatial development was recorded in both DC and pulsed modes of operation. A Princeton Instruments Intensified Charge Coupled Device (ICCD) camera model (ICCD-MAX) was used for this purpose. The temporal resolution of the ICCD camera system is 2 ns and can be used in the wavelength range from visible and down to 100 nm. The camera is controlled by an ST-133 controller that is controlled by an interface program (winview) supplied by the company. It can be operated either in a shutter mode (DC case) or in a gate mode (pulsed case). VUV images of the discharge were obtained with the whole system under vacuum, as shown in figure (4.12). According to the wavelength range, an optical filter is placed in the filter wheel. The lens used is a MgF_2 with a 5 cm focal length. The whole imaging system was evacuated using a turbo molecular pump. As for images in the visible range, a quartz window was used instead of the optical filter.
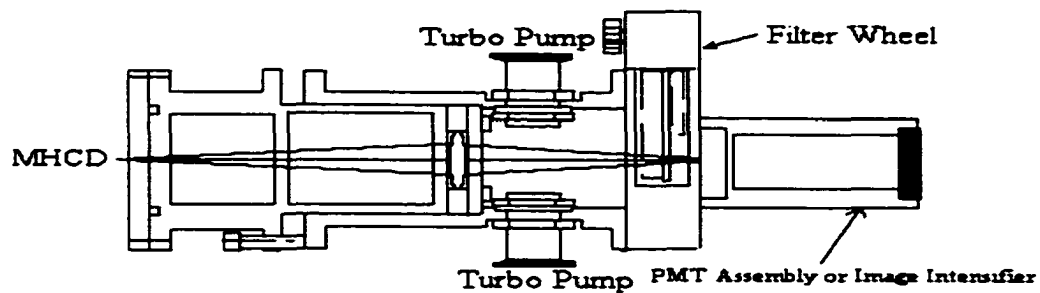
Figure (4.11) Setup for pulsed power measurements.
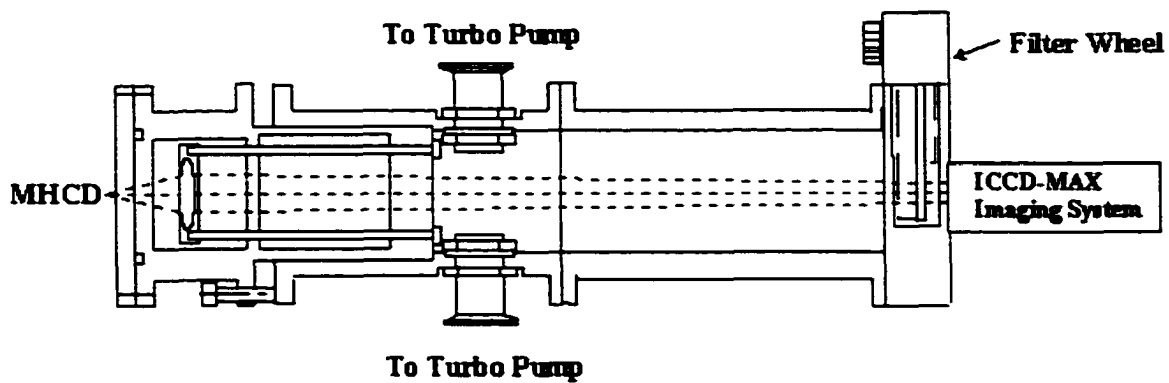
Figure (4.12) VUV and Visible imaging system.

CHAPTER V

RESULTS

Characterization of DC operation of Microhollow Cathode Discharge, both electrical and spectral, has been studied extensively. In this chapter, results of pulsed excimer emission from MHCD in xenon (Xe) and argon (Ar) will be presented. Electrical and spectral measurements of DC operation were repeated in order to relate it to the pulsed measurements.

5.1 DC Operation of MHCD

5.1.1 DC MHCD in Xenon [39,57-59]

Previous measurements of DC MHCDs in rare gases focused on characterization of the excimer source both electrically (I-V characteristics) and optically (spectral and absolute power measurements). Another characteristic is the spatial distribution that allows studying the excimer power density and its dependence on both pressure and current. This can be achieved by recording VUV images of the source as a function of both discharge current and gas pressure. The spatial distribution of VUV excimer radiation was measured using the ICCD-MAX system.

An I-V characteristic was measured for MHCD with sample configurations of 250 μm hole diameter, electrode thickness of 100 μm, and a 250 μm thick dielectric. Typical for a MHCD, the I-V characteristics can be divided to three regions: a) the positive resistive, which is referred to as Townsend discharge; b) a negative differential resistive part due to hollow cathode effect; and c) normal glow discharge as can be seen in figure (5.1), where the I-V characteristics and

the VUV output power of MHCD in 400 Torr xenon dependence on current are shown. In the normal glow discharge region, the sustaining voltage is in the range of 200-250 V depending on the excimer gas and pressure range. The radiant power measurements of VUV excimer radiation at 172 nm showed a linearly increasing radiant power with increasing current. In DC experiments, the current was limited to 8 mA to avoid thermal damage of the sample.

To study the spatial distribution of the VUV excimer source and its dependence on both pressure and current, the imaging system setup described in chapter IV was used and adjusted for a magnification ratio of 10. For DC images, the current was kept below 8 mA, and the pressure was changed in the range of 100 to 760 Torr. Figure (5.2) shows VUV images of a 400 Torr xenon discharge with the current as a parameter. These images show that at low DC current, while the discharge is still in the positive resistive region, all the VUV radiation is concentrated within the hole forming a ring with a thickness of about 40 μm [57,58]. At very low currents, it starts as a part of a ring and starts to fill the ring with increasing current. Further increasing of the current results in switching the discharge to the negative resistive mode. In this mode, the VUV excimer radiation starts to spread out of the cathode hole and over the cathode surface, and the excimer source increases with further increasing of the current. This increase of the source size would explain the increase of the radiant power with current.
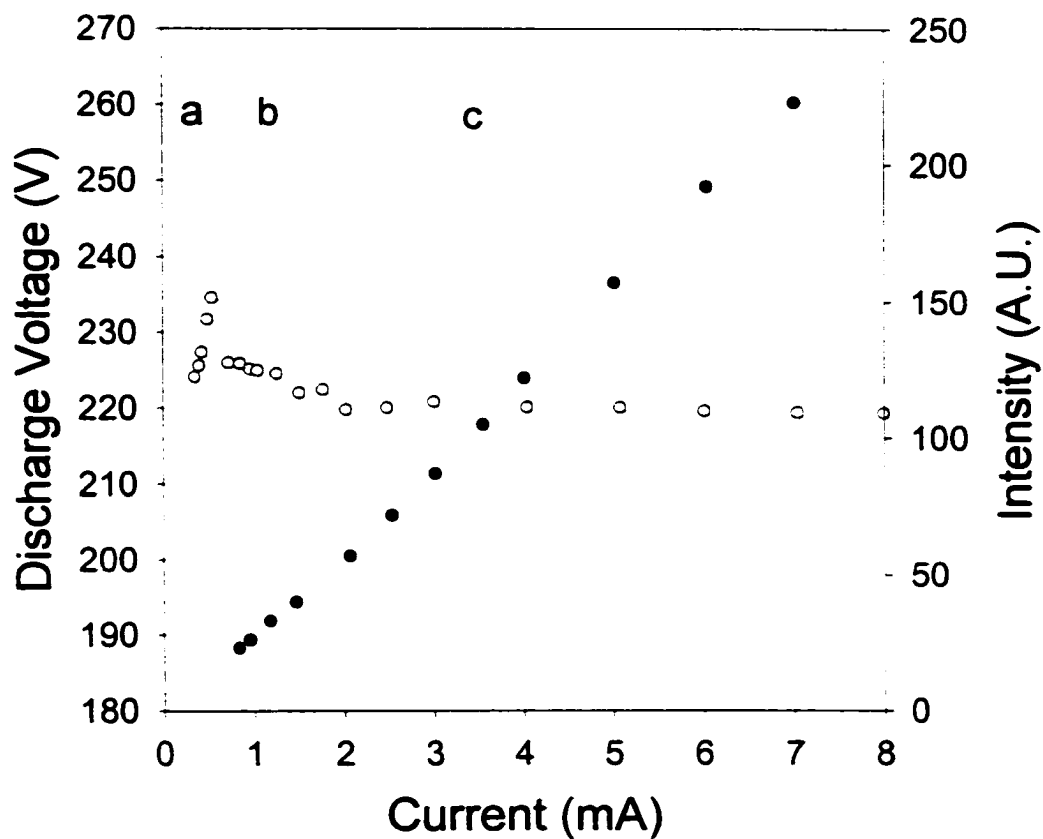
Figure (5.1) IV characteristics for MHCD in 400 Torr xenon for a hole diameter of 250 μm. The voltage (hollow circles) has (a) positive resistance at low current, (b) negative resistance, and (c) constant at higher currents. The Intensity (solid circles) increases linearly with increasing current.

1 mm

| 0.5 mA | 0.8 mA | 1 mA |

| 2 mA | 4 mA | 6 mA |
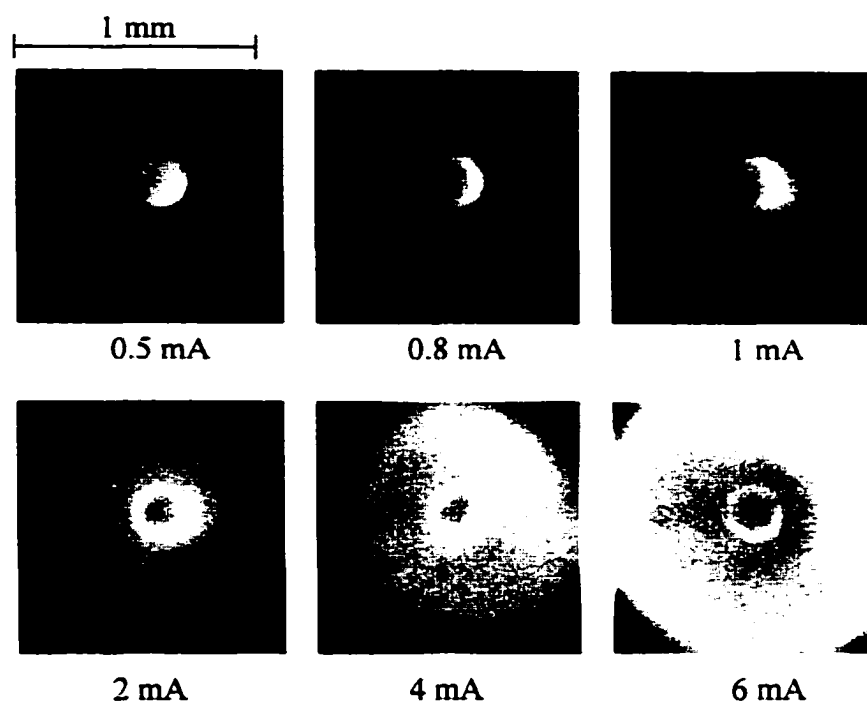
Figure (5.2) End-on VUV images of MHCD at 400 Torr xenon. At low current the discharge is constrained in the hole and expands outside the hole on the cathode surface with increasing current.

In addition to the current dependence of the excimer source, another parameter controlling the source size, gas pressure, was studied. Figure (5.3) shows the pressure dependence of the VUV excimer source on the gas pressure for a DC current of 3 mA in xenon discharge. While increasing the gas pressure from 200 to 760 Torr at a constant current of 3 mA decreased the source size, it increased the discharge. Using these images, a VUV excimer radiation profile was evaluated, and the radiant emittance defined as the power per unit source area was obtained. Figure (5.4) shows a radiant emittance profile dependence on pressure at a constant current of 3 mA in Xe discharge where the radiant emittance increased with increasing pressure up to 2 W/cm^2 at atmospheric pressure [59].

5.1.2 DC MHCD in Argon

Moving towards shorter wavelength argon is another excimer gas with excimer emission at 127 nm that was studied for excimer emission. Experiments have been performed for both static and flowing gas in both DC and pulsed modes.

5.1.2.1 DC Discharge in Static Argon [60]

Spectra of a DC MHCD in static argon showed the excimer continuum peaking at 127 nm with features at 130 nm, which indicated superimposed line radiation. Two different dielectrics were used in these experiments, mica and alumina, and the spectra were obtained with a spectral resolution of 2 nm. Figure (5.5) shows the spectral emission of MHCD in static argon. The position of this line radiation in the spectrum pointed towards oxygen as impurity. Atomic oxygen
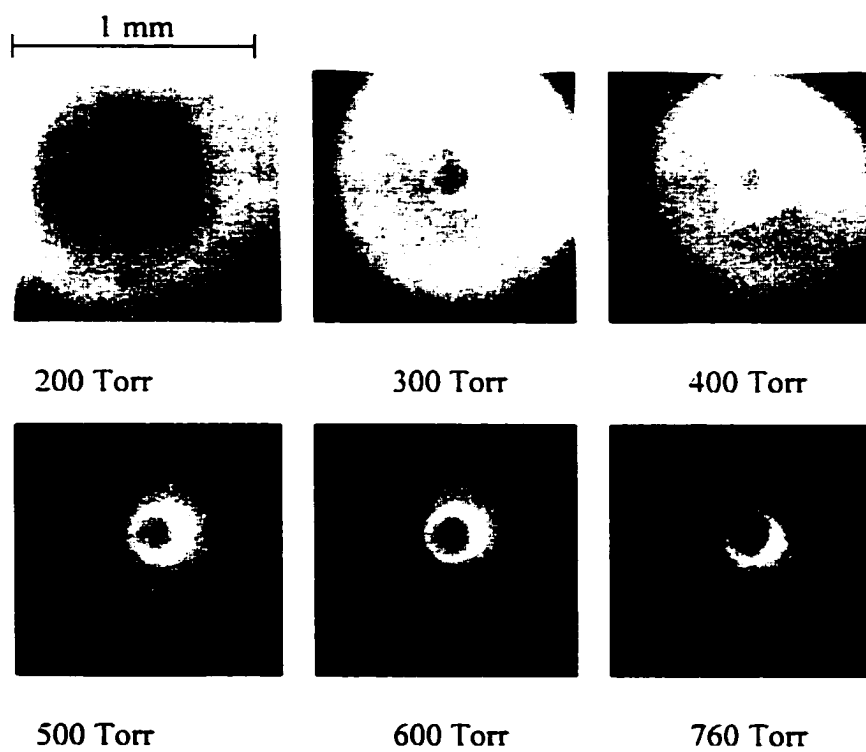
Figure (5.3) End-on VUV images of MHCD in xenon at 3 mA for different pressures. The excimer source size decreases with increasing pressure for a constant current.
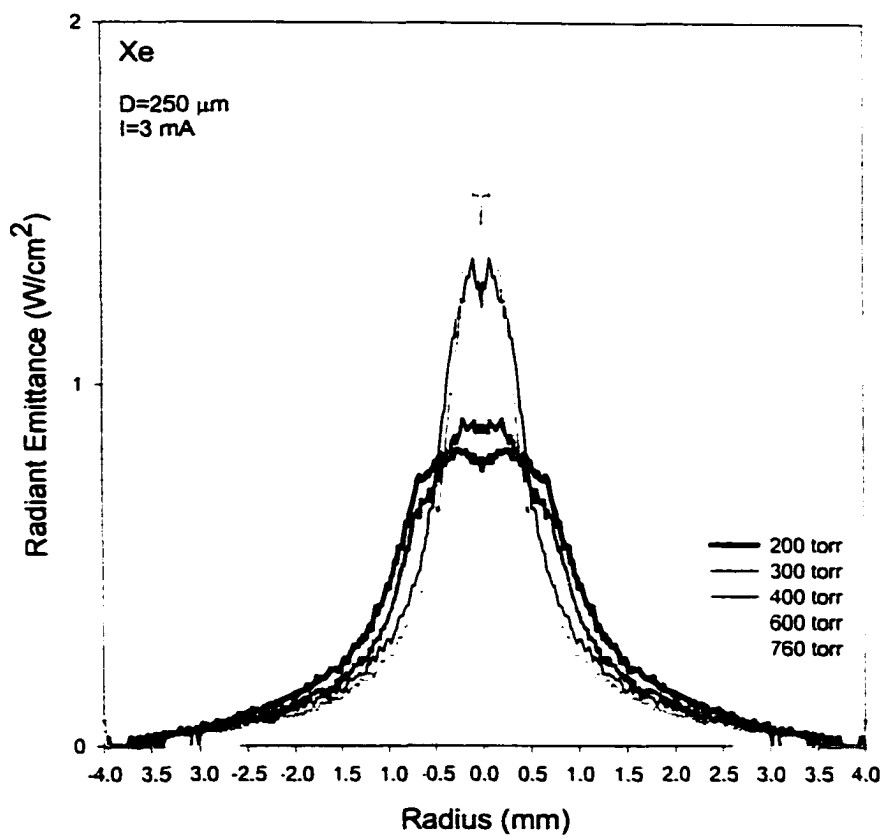
Figure (5.4) Radiant emittance profile of MHCD in xenon at 3 mA. The radiant emittance increased with increasing pressure.
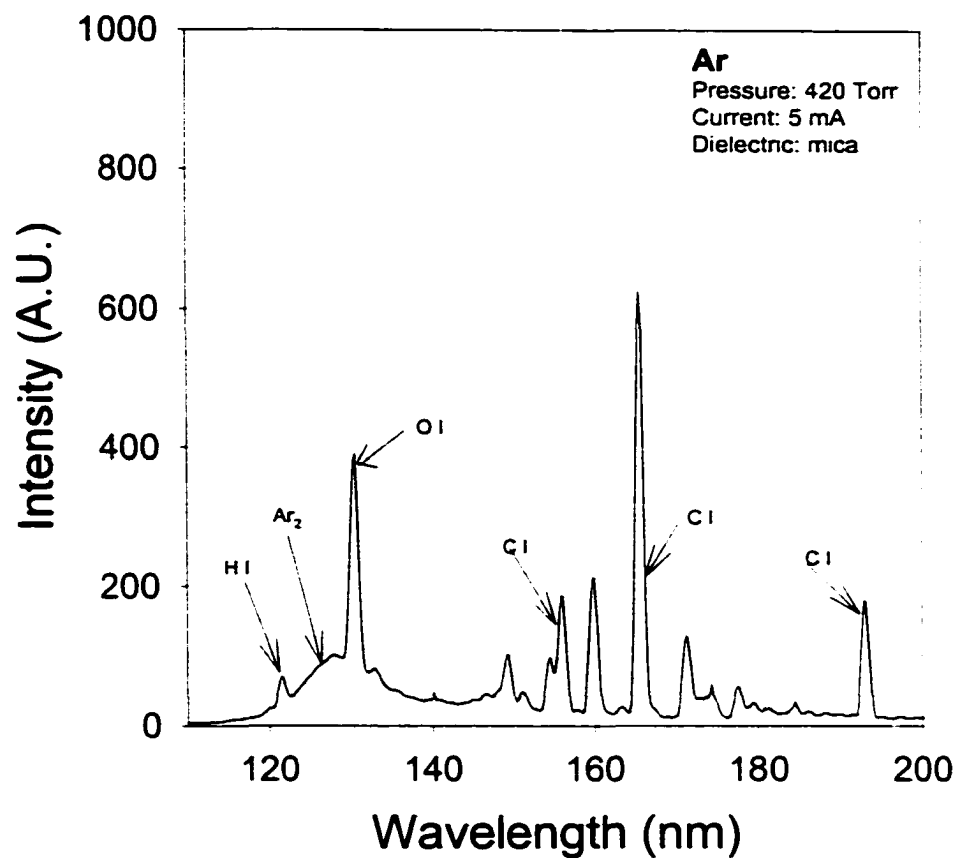
Figure (5.5) Spectral emission of MHCD in static argon with mica as a dielectric.

Impurity lines can be seen in the measured spectral range. The argon excimer

continuum peaks at 127 nm and is superimposed by an oxygen line at 130 nm.

is known to emit line radiation at around 130.4 nm. These transitions are components of the $2p^4 \; ^3P \leftarrow 2p^3(^4S^0)3s\,^3S^0$ triplet at 130.2 nm, 130.5 nm, and 130.6 nm. Collisional dissociation of molecular oxygen in an argon discharge with added oxygen was expected to provide a high concentration of atomic oxygen, and a resonant transfer of energy to the oxygen atom by the argon dimer is likely. This would provide a source of line radiation, rather than excimer radiation with its relatively broad emission spectrum. In order to study this effect, the spectral emission of microhollow cathode discharges and the spatial distribution of the VUV source in well-defined argon/oxygen mixtures were measured.

The sample electrodes thickness was 100 μm, separated by a 250 μm dielectric layer, and with circular holes of 100 μm diameter. In this experiment, alumina, rather than mica, was used because of its tolerance to high temperature operation. The discharge was operated in a direct current mode, with sustaining voltages between 200 V and 300 V and currents in the two to ten mA range. The discharge gas was argon at high pressure, up to 1100 Torr, with admixtures of oxygen below 1%.

Measurements of the spectral distribution in pure argon (research grade) and evacuation of the discharge chamber revealed that even in this case impurities determined to a large extent the emission in the studied VUV range from 120 nm to 200 nm. With alumina, line radiation at 130 nm contributed, even for pure argon filling, to approximately 20% of the total optical power in the range from 120 nm to 140 nm, as shown in figure (5.6) where the ratio of the oxygen line to the excimer continuum peak is higher than that when mica was used as a
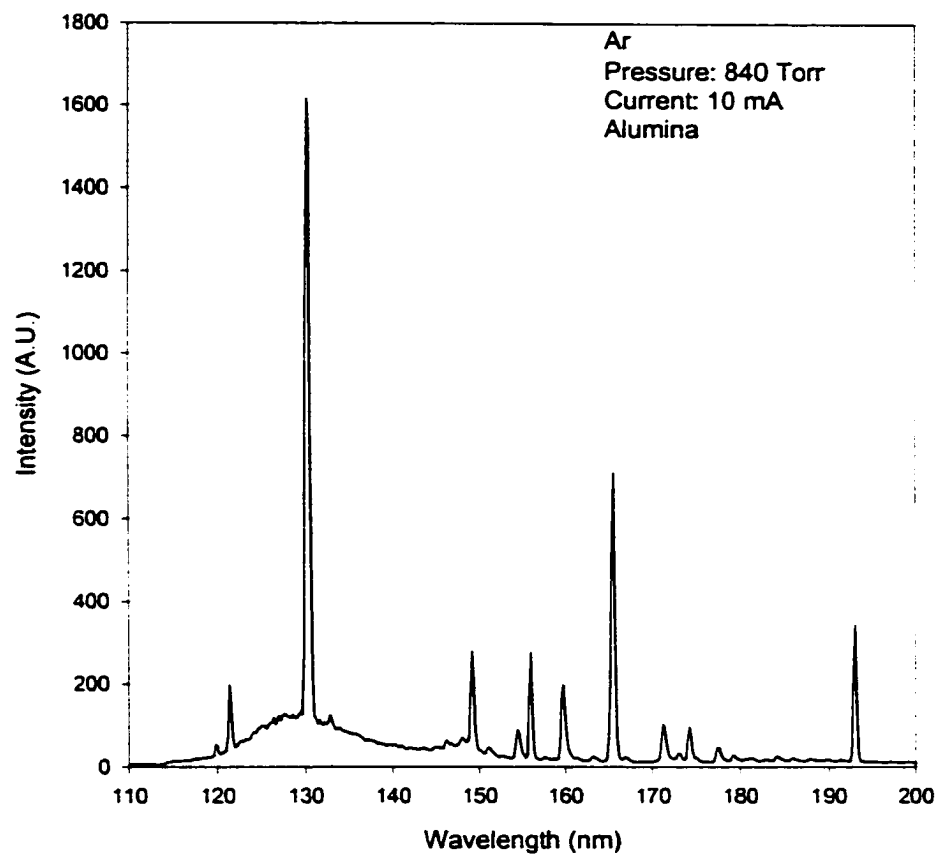
Figure (5.6) Spectral emission of MHCD in static argon with alumina as a dielectric. The ratio of the oxygen line intensity to the excimer continuum is higher than the case of mica.

dielectric. Spectra in a limited spectral range (129 nm to 132 nm) with the best spectral resolution achievable with the present diagnostic system ($\Delta\lambda \sim 0.2$ nm) showed two peaks at 130.2 nm and 130.5 nm shown in figure (5.7). The second line is asymmetric, indicating the presence of a third line, which can't be resolved due to the resolution. This spectrum, therefore, seems to correspond to the atomic oxygen transitions $2p^4\ {}^3P \leftarrow 2p^3({}^4S^0)3s\ {}^3S^0$ triplet.

At high pressures of about 1100 Torr, the impurity lines, except the oxygen lines at 130.2 and 130.5 nm, become more dominant, which is shown in figure (5.8) (upper section) where the VUV spectrum of an MHCD in argon is shown for a pressure of 1100 Torr, compared to 830 Torr as in figure (5.6). With oxygen added, the intensity of the oxygen emission increases at the expense of the argon excimer emission (figure (5.8), lower sections) [60]. It reaches a maximum at approximately 4 Torr oxygen added to argon at 1100 Torr, corresponding to 0.36%. With increasing oxygen, not only the argon excimer radiation disappeared, but also the other oxygen lines in the spectrum almost vanished. However, at an admixture of 10 Torr oxygen to the 1100 Torr argon, molecular oxygen emission at 185 nm begins to emerge. The studies on the effect of various concentrations of oxygen in argon at a given pressure were performed at a discharge current of 10 mA. Reducing the current to the lowest possible current value of 2 mA (below that the discharge could not longer be sustained) for the same pressure showed a linear decrease in atomic oxygen emission with current.
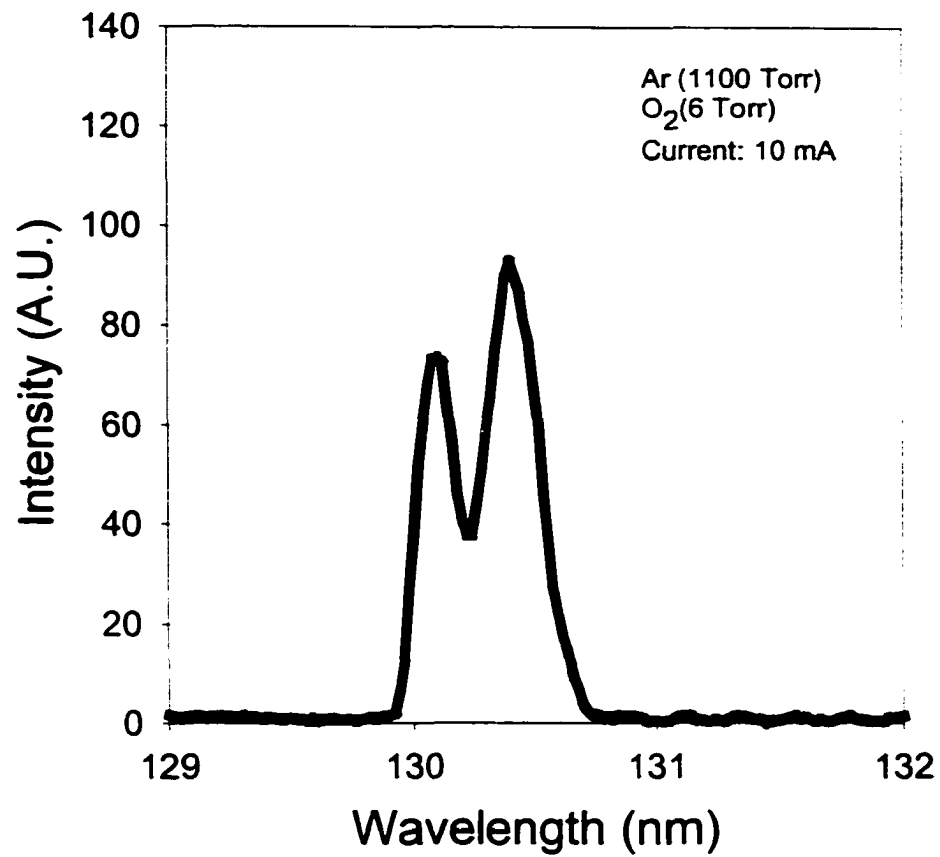
Figure (5.7) Oxygen lines at 130.2 and 130.5 nm. The second line profile is slightly asymmetric indicating the presence of a third line.
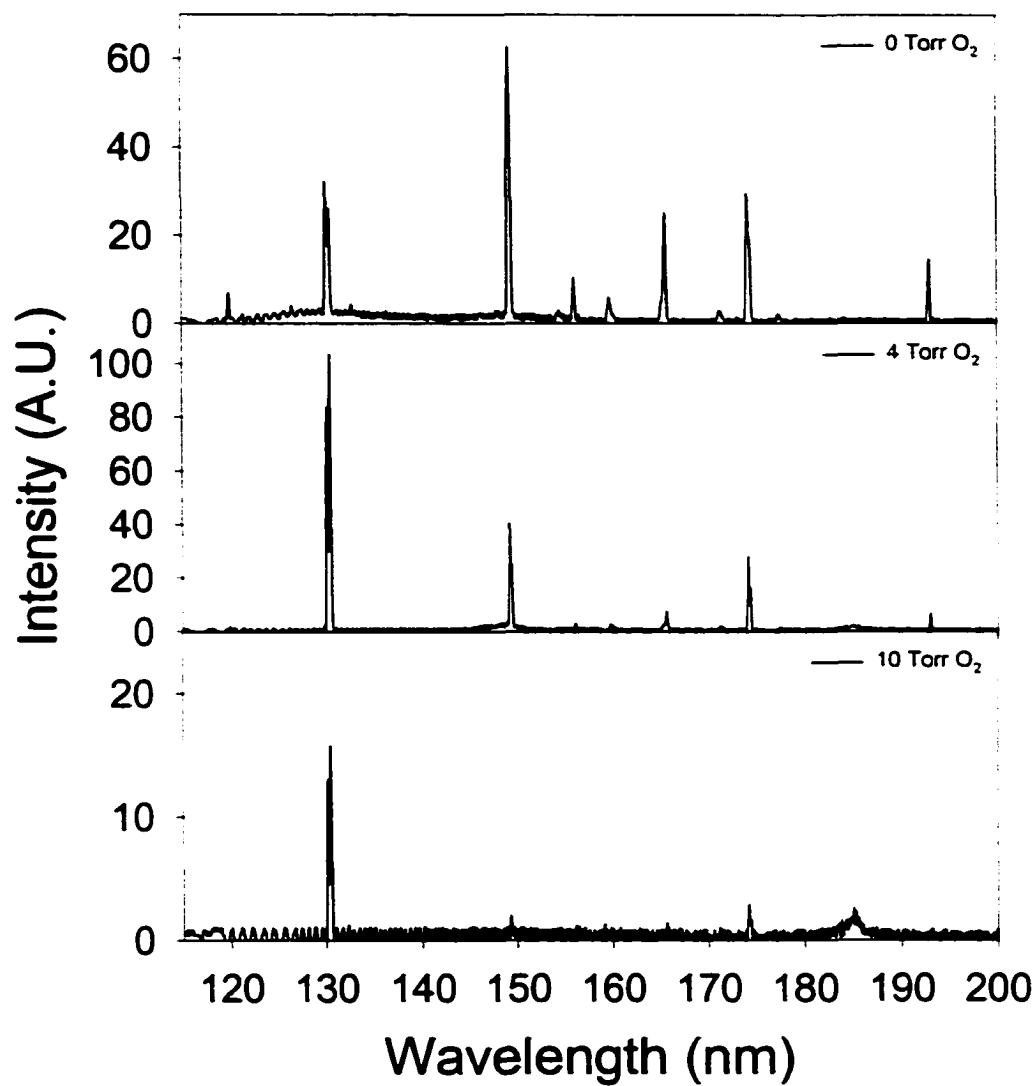
Figure (5.8) Spectral emission of MHCDs in argon at 1100 Torr with increasing concentration of added oxygen. The oxygen lines at 130.2 nm and 130.5 nm reach a maximum intensity at 4 Torr of oxygen added to 1100 Torr of argon [60].

Assuming that the emission is isotropic, the internal efficiency of the oxygen emitter was found to be 0.7% at oxygen concentrations of less than approximately 0.1% in argon (at 1100 Torr and a discharge current of 10 mA). This corresponds to a total optical power of about 15 mW per microhollow cathode discharge in the range covered by the optical filter. The efficiency decreases with increasing oxygen concentration, and for oxygen concentrations of 0.9% it is only 0.2%, as shown in figure (5.9). The decreasing efficiency is in part due to an increase in sustaining voltage at constant current. For a 10 mA discharge, the sustaining voltage increases from 225 V for the case where no oxygen was added to approximately 300 V for 0.9% oxygen concentration.

5.1.2.2 DC Discharge in Flowing Argon

Due to impurities in static argon operation, the excimer efficiency was lower than 1% and consequently a higher purity is required. This can be achieved by flowing the gas at a constant flow rate, which can be controlled using a flow meter such that the pressure is constant within the chamber. In early experiments, a Matheson flow meter was used to control the gas flow rate at about 175 sccm, but it produced some leaking and the impurity lines still appeared in the emission spectra, as can be seen in figure (5.10). The oxygen line was still visible over the excimer continuum, and both the line and continuum intensities increased with increasing pressure. So a mass flow controller model MFC-8160 was used, which is vacuum tight and presents no leaks. Flowing argon at a much lower rate of 40 sccm controlled by the MFC8160 flow meter improved the excimer emission, and almost all the impurity lines disappeared in
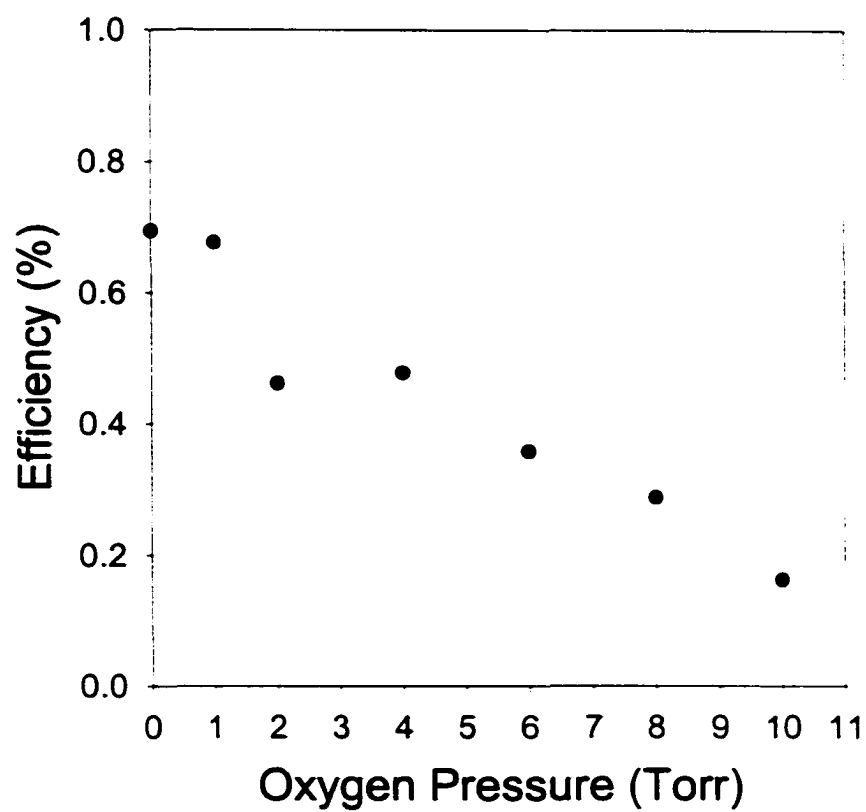
Figure (5.9) Excimer efficiency for different oxygen ratios added to argon at a pressure of 1100 Torr at 10 mA.
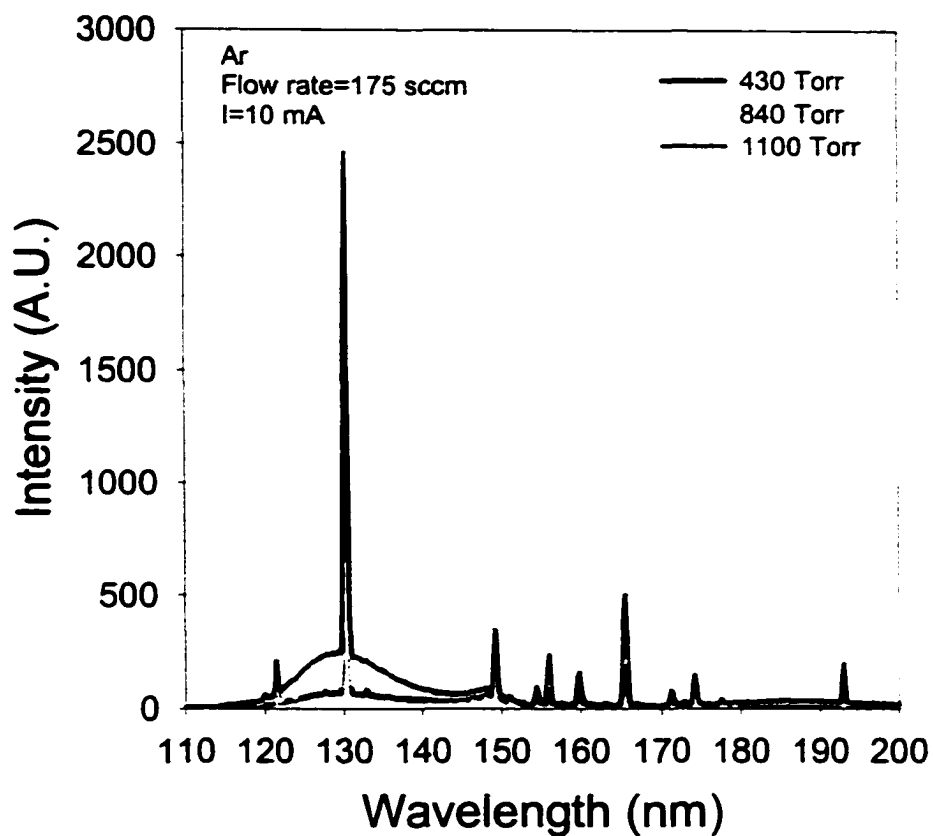
Figure (5.10) Flowing argon excimer emission for different pressures using the Matheson flow meter. The oxygen line still existed and the excimer continuum increased with increasing pressure.

the range of 110 to 200 nm except for a small oxygen peak over the excimer continuum, as shown in figure (5.11).

Power measurements were taken using a calibrated photodiode SXUV-100 and showed an increasing power with increasing pressure up to 1100 Torr and almost linear dependence on current. Figure (5.12) shows VUV total radiant power for argon with a flow rate of 40 sccm dependence on both pressure and current assuming an isotropic emission. From these power measurements, the efficiency of VUV excimer radiation of the argon discharge was calculated to be increasing with increasing pressure and tends to saturate at pressures higher than atmospheric, as shown in figure (5.13). At a pressure of 1100 Torr and a DC current of 3 m, an efficiency of 6% was measured, which is more than 6 times the case of static argon. This shows that the excimer radiation is highly affected by contamination produced by leaking or from the sample itself. Flowing the gas helped to reduce the concentration of this contamination.

5.2.1.3 VUV Imaging of DC MHCD in Flowing Argon

Similar to the xenon discharge, VUV images of MHCD in flowing argon showed the same behavior and dependence on current, as can be seen in figure (5.14a). For argon at atmospheric pressure and flowing at a rate of 40 sccm, at low current, while the IV characteristics are in the positive resistive part, the VUV radiation is restricted to the hole. With increasing current, the discharge starts to expand on the cathode surface. An intensity profile, figure (5.14b), shows that the intensity increases with increasing current and spreads over the cathode area.
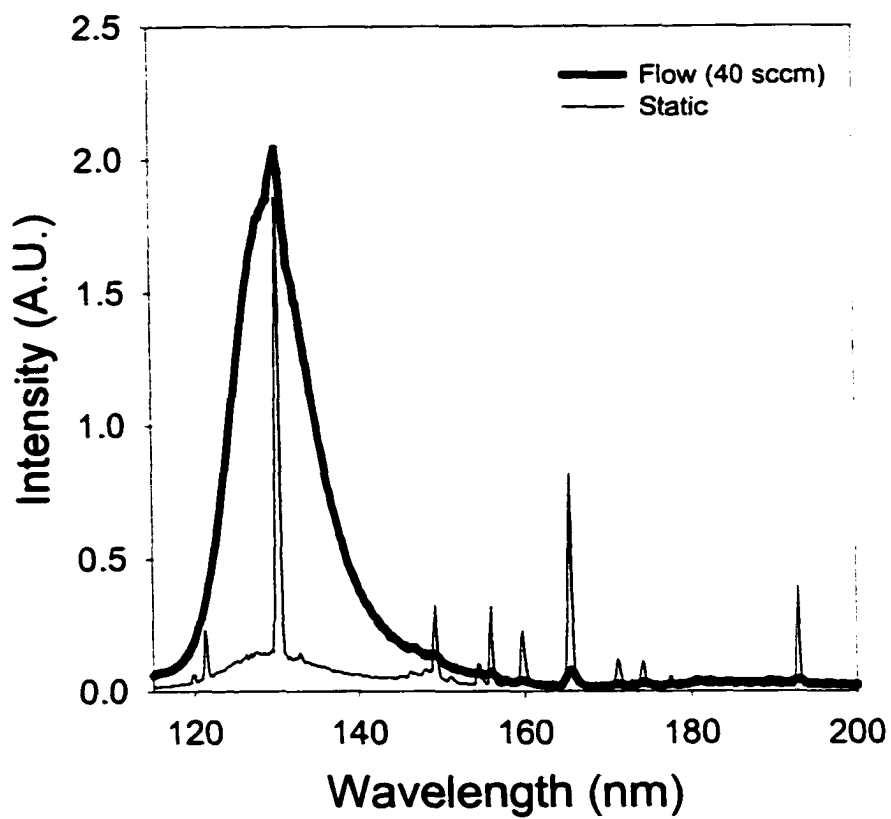
Figure (5.11) Excimer spectrum of argon MHCD with flowing and static argon. Flowing argon increased the excimer continuum, and all the impurity lines decreased.
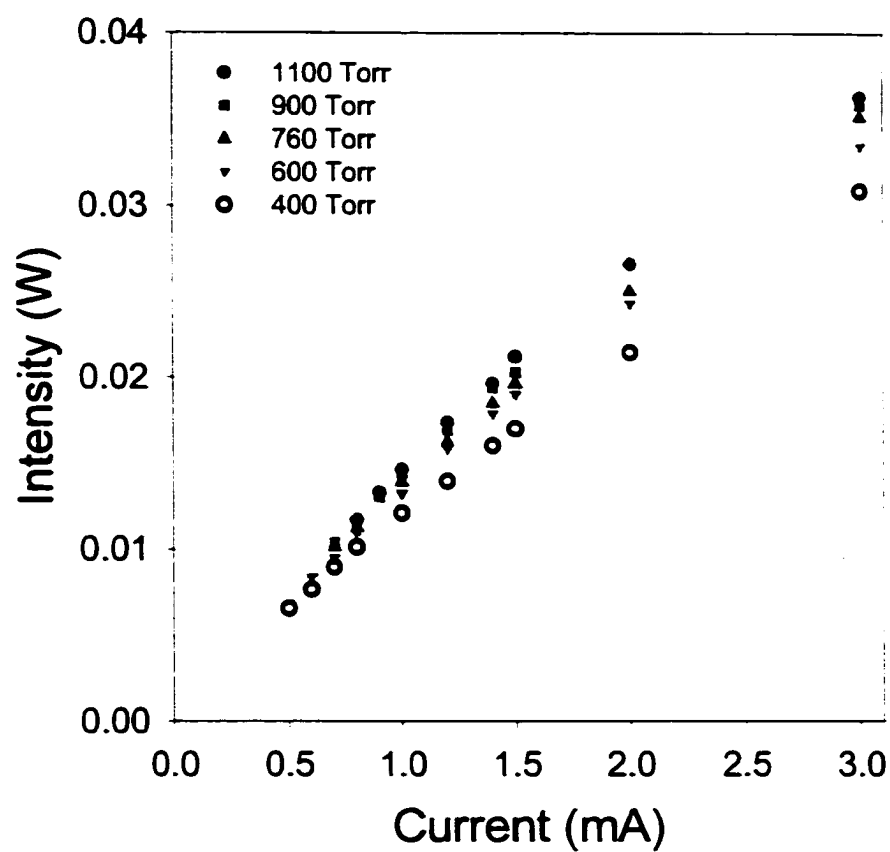
Figure (5.12) The VUV intensity is linearly increasing with current and increases

with increasing pressure at a constant flow rate of 40 sccm of pure argon.
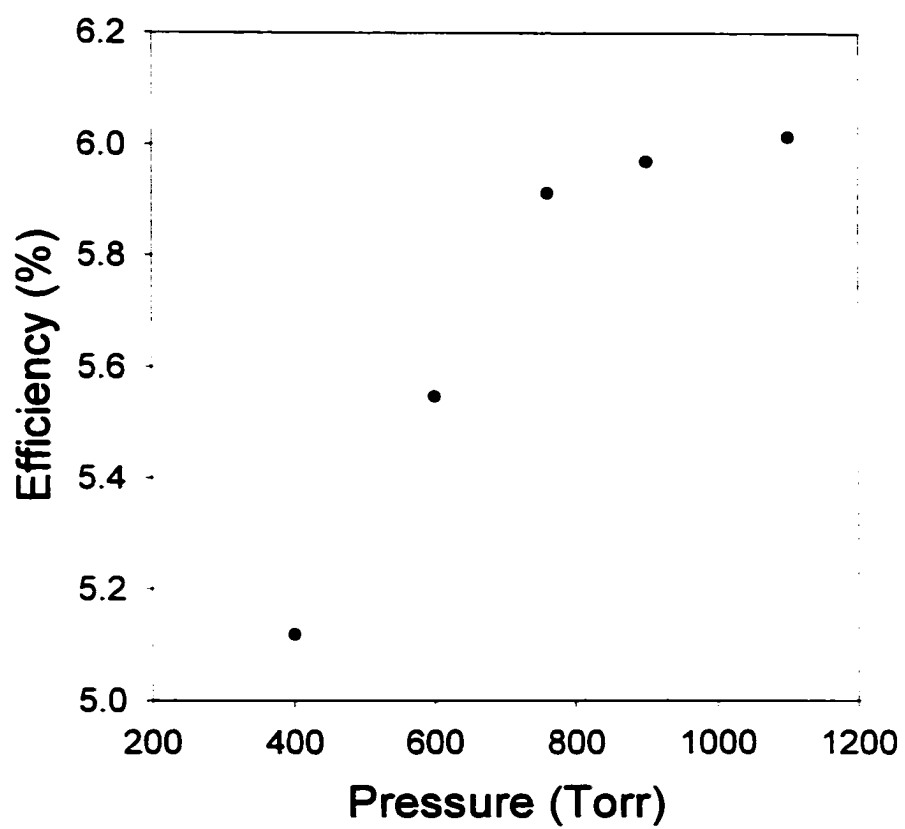
Figure (5.13) Argon excimer emission efficiency increases with pressure and approaches a constant value of 6% at 1100 Torr at 3 mA.

| 2.5 mA | 2 mA | 1.5 mA |

| 1 mA | .75 mA | .55 mA |
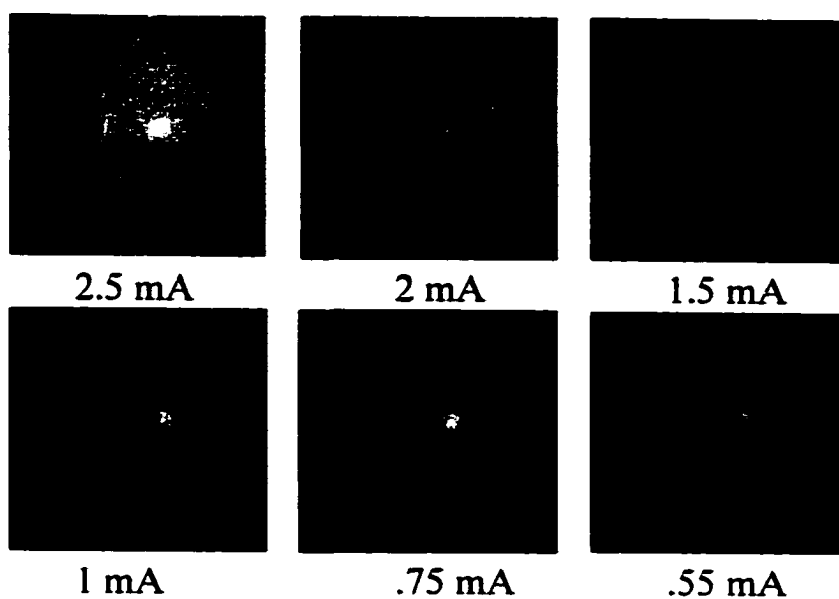
Figure (5.14a) The excimer source size increases with increasing current in argon MHCD.
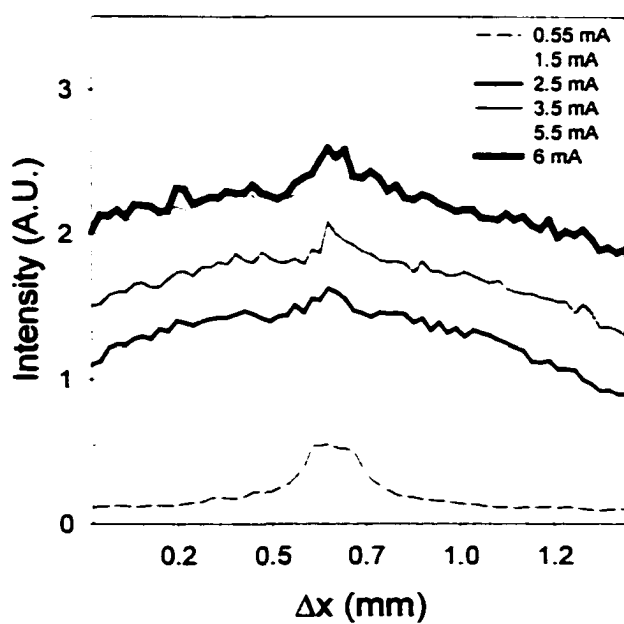
Figure (5.14b) The intensity profile of VUV emission in MHCD in argon. The intensity increases with increasing current and close to uniform over the surface.

5.2 Equilibrium Pulsed Operation in Xenon [39,61-63]

The current in DC operation was limited to avoid thermal damage of the sample, and an alternative to increase the current was pulsing the discharge with long pulses so it would allow increasing the current without increasing the average electrical power. The pulse width used in these experiments is 0.7 ms at a pulse repetition rate of 10 Hz. This operation allowed us to increase the current up to 80 mA. No further increase was possible because the discharge became unstable, and high current pulses accompanied by very low excimer radiation corresponding to arc discharge started to appear. The pulse width in this case is long enough for the discharge to reach steady state. By increasing the current to 80 mA the output VUV excimer power is still linearly increasing with increasing current, as shown in figure (5.15). In the same figure, it is shown that the sustaining voltage of the discharge stays constant, 225 V for 400 Torr xenon. Consequently, the internal excimer efficiency is constant and equal to the DC mode of about 6 to 9%, independent of current.

In this mode of pulsed operation, due to the large size of the excimer source, a one to one imaging system was used, and end-on VUV images of the excimer source were recorded. By synchronizing the camera to the triggering pulse of the discharge, the images were taken in the middle of the pulse (300 μs from the beginning of the pulse) with an exposure time of 200 μs. In "ms" pulsed operation, VUV images showed a similar dependence of MHCD excimer source size on pressure and current as in the DC case. Figure (5.16) shows VUV images of the excimer source observed end-on with pressure and current as
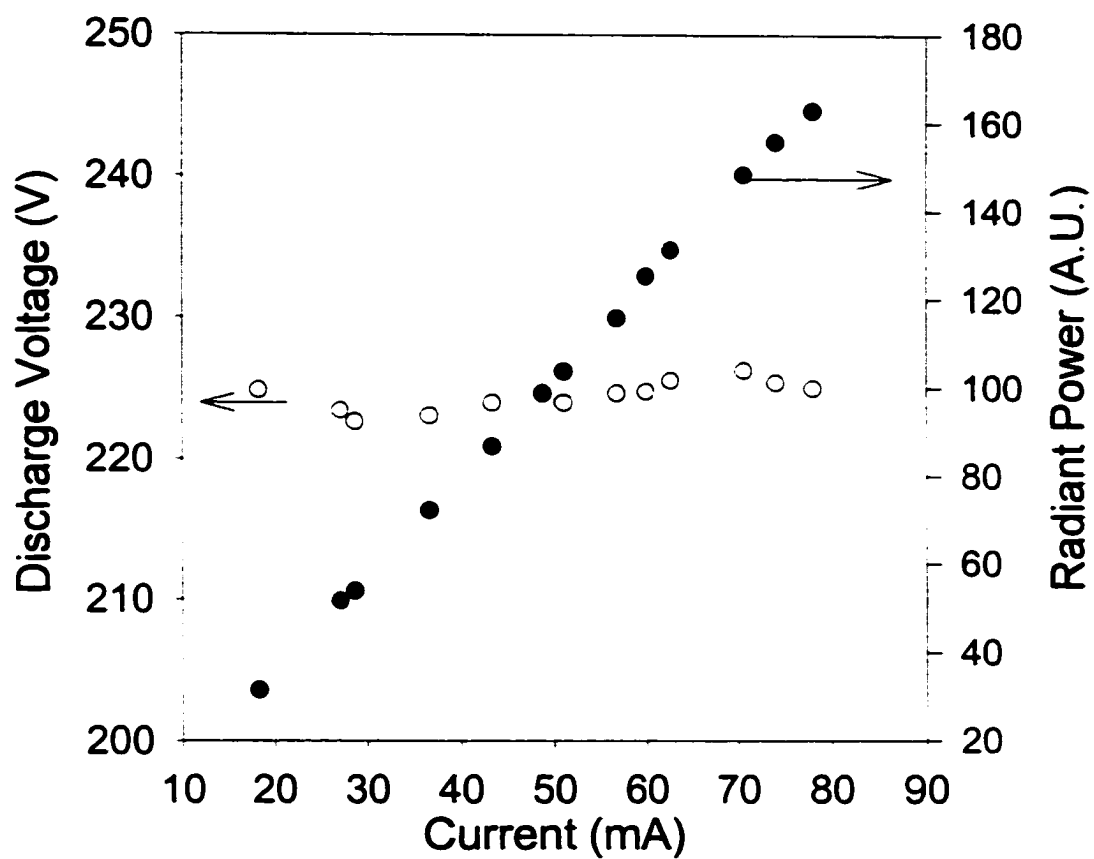
Figure (5.15) In pulsed operation, the steady state voltage (open circles) is constant with increasing current resembling a normal glow discharge. The intensity (solid circles) is increasing with increasing current.
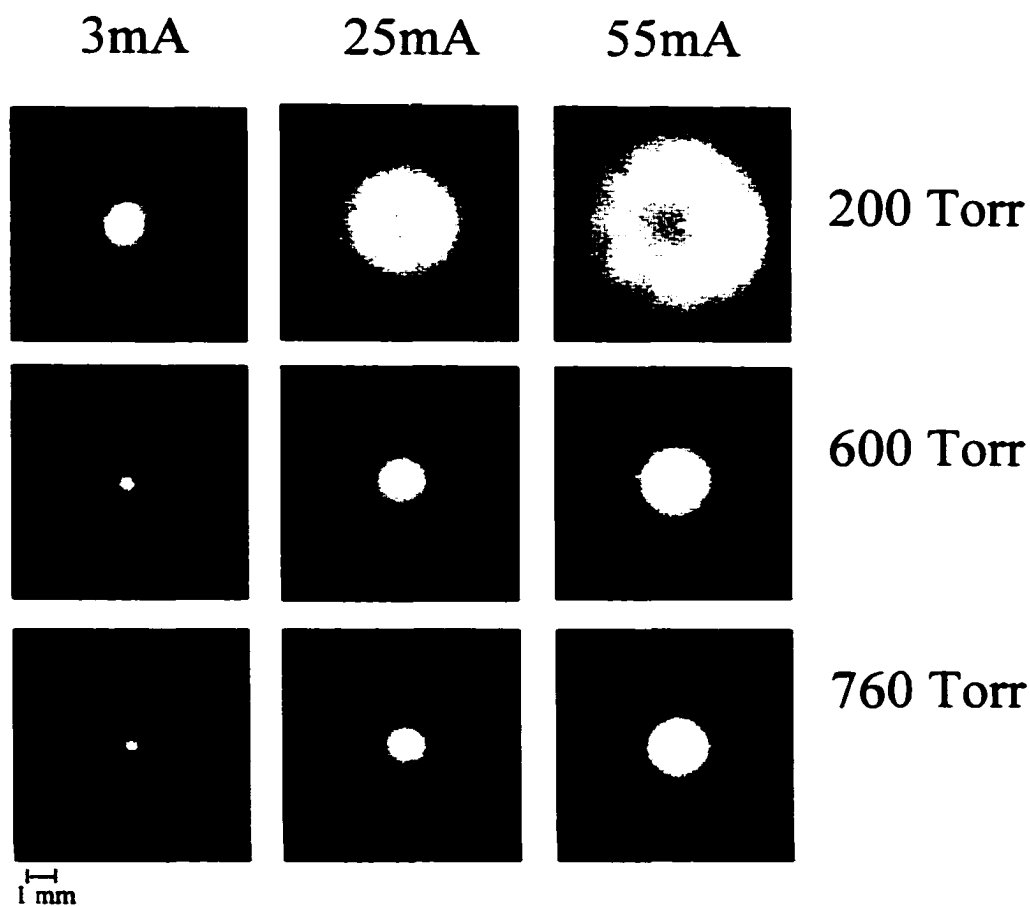
Figure (5.16) End-on VUV images of pulsed operation for different currents at different pressures. Similar to the DC, case the source size increases with increasing current and decreases with pressure.

parameters. Combining both DC and pulsed current measurements with the VUV images showed that at a constant pressure the spatially averaged current density, $j = 4i/\pi d^2$, where d is the diameter of the excimer source, stays constant. For example, for a 400 Torr xenon discharge, where it has maximum excimer efficiency, the averaged current density is 0.3 A/cm². On the other hand, for constant current, the current density increases linearly with the square of the pressure, $j = Cp^2$, where C is approximately 1 A/bar²cm². Both of these two relations, a current density being independent of the current and scaling with the square of the pressure, are typical for normal glow discharges [64]. Although the average current density was found to be constant, indicating a homogeneous spatial distribution of the radiative emittance (power per unit area), VUV images and images in the visible spectrum show an inhomogeneous distribution of the excimer radiation, as can be seen in figure (5.16, 5.17). The contrast of figure (5.17) at 70 mA pulsed current and 200 Torr xenon has been enhanced to demonstrate this effect. Whereas the intensity in the VUV decreases with reduced distance to the cathode opening (which is located right in the center of the luminous area), the intensity in the visible has maximum values in and close to the cathode hole area [63].

Side-on images in the visible range have shown that the thickness of the plasma layer, including both cathode fall and negative glow, is constant and in the range of 100-150 μm over the entire area.
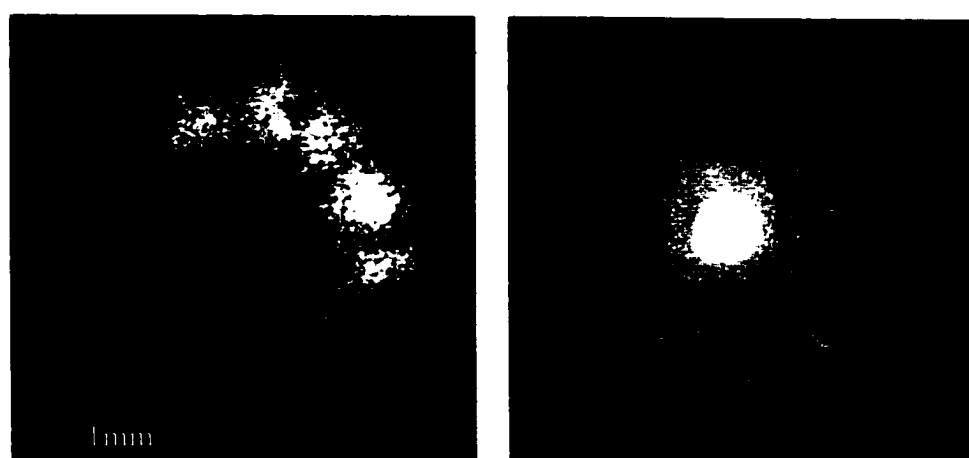
Figure (5.17) VUV (left) and visible (right) end-on images of xenon MHCDs at a pressure of 200 Torr and a current of 70 mA [63].

A pronounced feature in the images of the plasma in the visible (figure (5.17)) is channels extending from the central area to the plasma boundaries. These channels have been observed for most current and pressure conditions, except very low currents and very high pressures. Looking at the corresponding VUV images, these channels appear as areas of reduced excimer intensity. They represent plasma with higher gas temperature and electron density than the areas between them.

In these images, a dielectric layer determines the outer boundary of the plasma. When the plasma has extended to this dielectric, any increase in current leads to a transition from a normal glow to an abnormal glow, which the plasma prone to instabilities, limiting its use as an excimer source if the dielectric layer on top of the cathode is reached.

5.3 Non-Equilibrium Pulsed Operation of MHCD

5.3.1 Non-Equilibrium Pulsed Operation in Xenon [65-67]

For equilibrium pulsed operation, increasing the current increased the output VUV excimer radiation, but the efficiency remained equal to the DC case in the range of 6-9%. A promising method to increase the excimer efficiency in glow discharges is pulsed electron heating. Experiments in atmospheric pressure air [48] had indicated that extremely short pulses could affect the electron kinetics without heating the plasma. The pulsed electric field shifts the electron energy distribution to higher values and consequently causes a nonlinear increase in the excitation and ionization rates. This pulsed electron heating effect is considered to be responsible for the observed increase in the efficiency in

barrier discharge excimer lamps [12], where increases in efficiency by a factor of 3.2 were obtained.

Pulsing MHCDs into the nonequilibrium condition can be achieved with low pulsed voltages of few hundreds volts. The "ns" pulse generator described in chapter IV was used to generate pulses with pulse duration of 20 ns, with peak voltages up to 750 V. The voltage pulse generated with this system is shown in figure (5.18) [67]. The FWHM is 20 ns and the rise and fall times are 10 ns. The pulse was applied to a dc microhollow cathode discharge in 400 Torr xenon. The sustaining dc voltage was 230 V and the dc current was 1 mA. The pulsed electric field causes an instantaneous increase in electron density, which after the pulse decays through recombination with a time constant of several microseconds. The discharge voltage drops from 230 V to approximately 100 V after the pulse and only the beginning of the recovery to the dc sustaining voltage is shown in figure (5.18), which is related to the temporal development in electron density.

Figure (5.18) shows the temporal development of the excimer emission at 172 nm, the peak in the second xenon excimer continuum. The VUV radiation was spectrally resolved by means of a McPherson 302 and recorded with of a PMT (Hamamatsu R1533). Measurements of the pulsed spectral distribution showed that the electrical pulse did not affect the line profile, so the radiation at 172 nm is representative of the total optical power in the VUV. The measured excimer emission is delayed with respect to the electric pulse, which is due to the time delay of the PMT that was measured as 50 ns. The peak in excimer
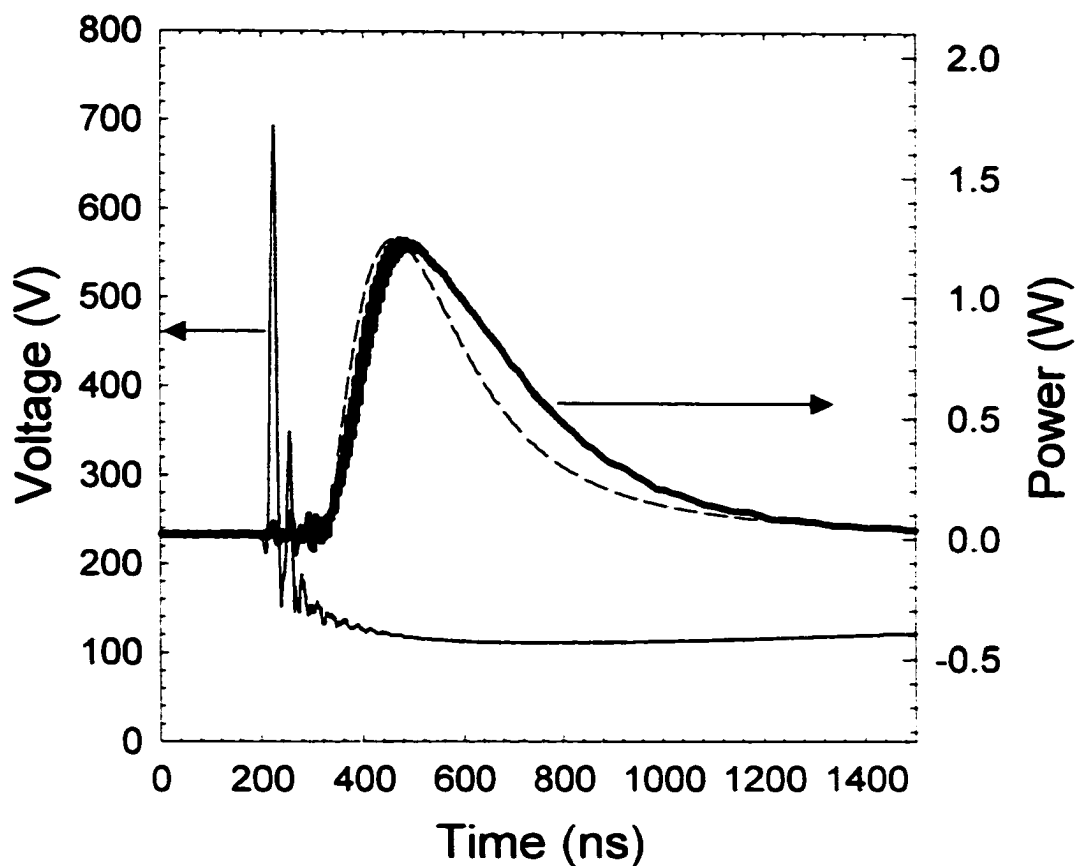
Figure (5.18) Temporal development of voltage across the microhollow cathode discharge and the corresponding xenon excimer emission at 172 nm. The voltage before pulse application (< 200 ns) is the sustaining voltage of the dc discharge. After pulse application, the discharge voltage drops to 110 V and approaches the dc value after several microseconds. The solid bold line represents the temporal development of measured excimer emission. The dc value of the excimer power (indicated by DC in the figure) is less than 2 % of the peak power. The dashed line represents the modeling results [67].

emission is at approximately 250 ns after the electrical pulse application. The FWHM of the excimer pulse is 350 ns, the decay time constant (1/e decay time) is 320 ns, and both are independent of pulse amplitude.

For a low peak pulse voltage up to 500 V, the excimer intensity stays at a constant value, the dc excimer emission. By increasing the amplitude of the pulsed voltage from 500 V to 750 V, the peak intensity increased exponentially, doubling every 50 volts. The absolute values of the optical power of the excimer pulse were obtained by measuring the excimer intensity at 1 mA dc with a calibrated detector and by relating this value to the value obtained by the temporal development of the emission, as shown in figure (5.18). Peak optical power is plotted versus peak voltage of the pulse in figure (5.19) [67]. Largest values are 2.75 W at a pulsed voltage of 750 V emitted from a single microhollow cathode discharge, which is more than two orders of magnitude compared to the DC case at 1 mA (20 mW).

In the case of pulsed operation, the efficiency is defined as the ratio of optical energy to electrical energy and is plotted in figure (5.19) versus voltage. The electrical energy was obtained by integrating over the temporal development of the product of voltage and current from the application of the voltage pulse to the time where the excimer pulse had decayed to about 10 % of its peak value. It was noticed that the efficiency decreases with increasing voltage up to 500 V from 8% to 4%. This is due to the fact that in this voltage range, the effect of the pulse on the excimer emission is negligible, but not the dissipated pulsed electric energy, which resulted in lowering the efficiency. Above 500 V the efficiency
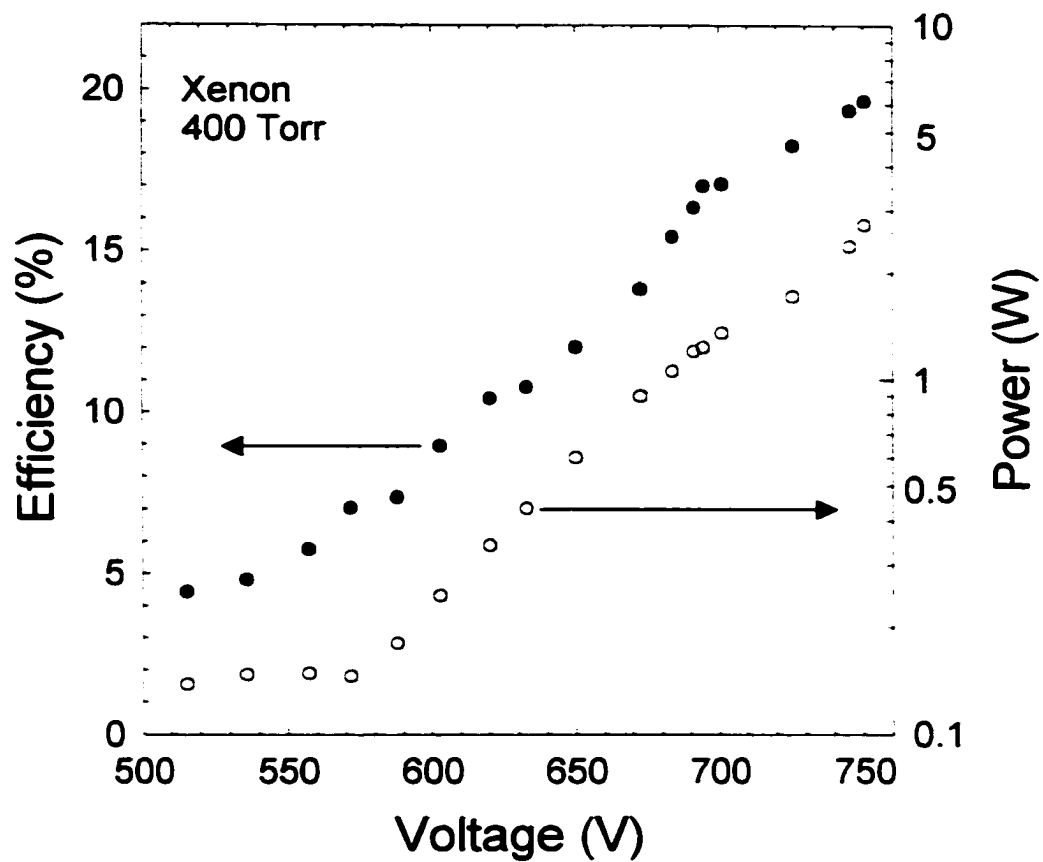
Figure (5.19) VUV optical power and corresponding excimer efficiency. Whereas the optical power increases exponentially, the efficiency increases linearly with pulsed voltage [67].

increases linearly with voltage and reaches 20 % at an applied pulsed voltage of 750 V, the largest voltage that our pulse generator provided.

Although the optical power increases exponentially, by a factor of 18 (0.15 to 2.75 W) from 550 V to 750 V pulses applied, the time averaged radiant emittance of the source rises only by a factor of 2.5 (from 5.9 to 15.2 W/cm^2). This is due to the fact that with increasing voltage and current, the area of the source expands. The diameter of the emitting area increases from 0.9 mm to 2.4 mm (diameter of pulsed radiation only) when the pulse amplitude is increased from 550 to 750 V. Temporally resolved photographs of the excimer source are shown in figure (5.20) where the exposure time was set to 300 ns, and the camera trigger was delayed 100 ns from the pulse, such that it is centered right at the time when the excimer emission peaked. In this figure, a VUV image of DC discharge at 1 mA (upper left) was recorded in order to see the effect of applying the pulse over the DC discharge. The hole size is 100 μm and is located in the center of the image. When the pulse is applied to the DC discharge, the area closer to the center (closer to the hole) becomes higher in intensity, and the diameter of this area increases with increasing pulse voltage.

Although the excimer lifetime of xenon excimers is known to be in the range of 0.09 to 0.14 μs [24,27], the intensity decays exponentially with a time constant of 320 ns. In addition to radiative decay, quenching processes may be involved, and as a result, the decay would be faster. The rate equation for excimer decay is given by:
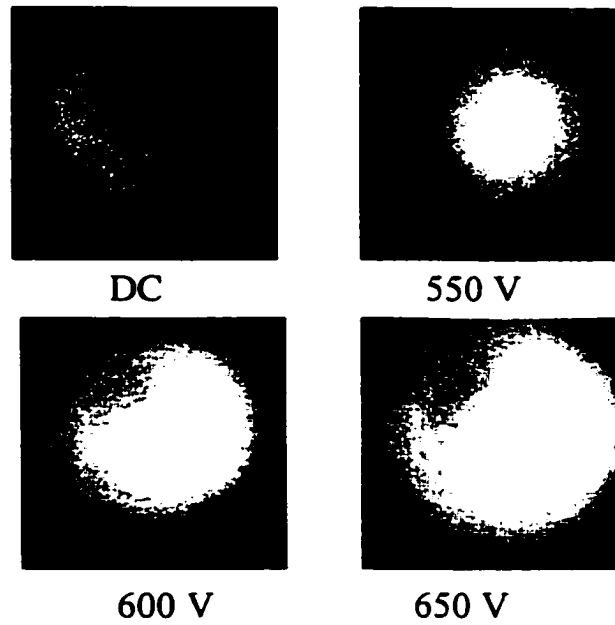
Figure (5.20) VUV end-on images for "ns" pulsed operation. At low peak voltage pulse, a higher intensity area is superimposed over the DC. With increasing pulse voltage, both the diameter and the intensity of the superimposed area increase.

$$\frac{d[X_2^*]}{dt} = -[X_2^*] \cdot \left(A_{ik} + \frac{1}{k_q[q]} \right)$$
(5.3)

where X_2^* is the excimer density, A_{ik} is the inverse spontaneous lifetime of the gas excimers, and $k_q[q]$ is the sum of all quenching rates. According to equation (5.3) and an exponentially decaying intensity, the total decay time constant (τ) is given by:

$$\frac{1}{\tau} = A_{ik} + \frac{1}{k_q[q]}$$
(5.4)

Taking this into consideration, the quenching processes rate was -0.145 μs for an excimer lifetime of 0.1 μs. This is not possible and can be due to a slower excimer formation process resulting in three-body collisions with the excited atoms produced by the recombination of molecular ions, which would affect the decay process.

5.3.2 Non-Equilibrium Pulsed Operation in Argon

"ns" pulsed operation in flowing argon generated an increase in the intensity compared to DC operation, however, not as high as that in xenon. In argon, the peak intensity was only about five or six times that of the DC case, while in xenon it was almost two orders of magnitude higher. Figures (5.21) show the intensity pulse for different pulse voltages at 1100 Torr and 3 mA with a flow rate of 40 sccm. For "ns" pulsed operation, the current was found to be mainly a capacitive current. This was verified by integrating the current pulse. The calculated capacitance according to:

$$V = \frac{1}{c} \int i(t) dt$$
(5.5)
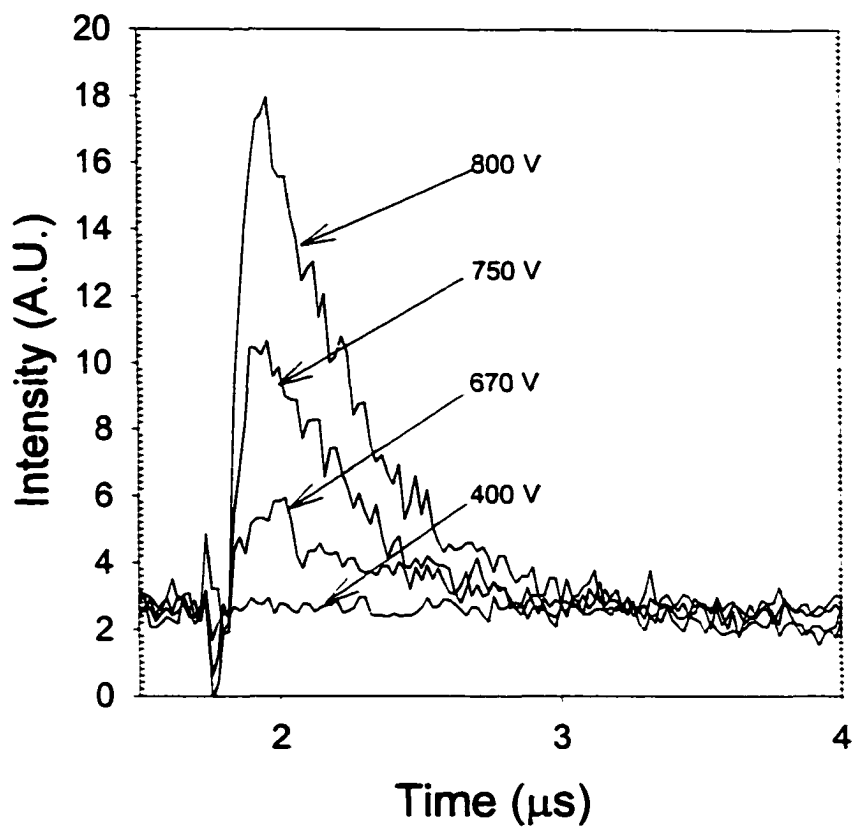
Figure (5.21) VUV excimer intensity and its dependence on the peak pulse voltage for "ns" pulsed operation in 1100 Torr argon MHCD and a 3 mA DC current.

was found to be 7 pF. Comparing this value with the calculated sample capacitance of 10 pF confirm this observation. When a 10 ns pulse was applied to the DC discharge, the VUV intensity increased exponentially with pressure. However, breakdown was reached at a pulse voltage of 800 V. Breakdown caused a high current pulse, thermal plasma, so no higher voltage was applied. The internal efficiency in this case is equal to or lower than in the DC case. Decreasing the pulse width would allow increasing the pulse voltage without breakdown, however the bandwidth limitation of the measuring equipment such as probes and oscilloscope limited the operation to 10 ns.

Following the same concept to calculate the quenching rate in argon as in xenon equation (5.4) was used with argon excimers lifetime of 3.4 μs as an average to the known lifetime range of 2.8 to 4 μs [24-28]. The intensity decays exponentially with a time constant of 500 ns and so the quenching processes rate was found to be 0.56 μs. Quenching is therefore six times more effective than radiative decay. By varying the pulse voltage in the range of 600 to 800 V the quenching rate ranged between 0.5 and 0.6 μs, which is expected since quenching is dependent on the gas temperature and by applying "ns" pulses only electrons are heated without increasing the gas temperature.

5.4 Electron Density of MHCD in Argon

The electron density was measured by measuring Stark broadening of the Hydrogen-beta (H_β) at 486.1 nm. A line profile of the system is obtained by recording an atomic line of a mercury lamp. The nearest mercury line to the required range was 435.8 nm. The spectral measurements were performed using

a 0.5 m McPherson monochromator with a grating blazed at 250-600 nm with a groove density of 2400 G/mm and the ICCD-MAX camera system at the exit slit for capturing the spectra. The measured mercury line was best fitted by a lorentzian profile, and the FWHM was found to be 0.32 A°. For pure argon discharge no hydrogen emission was detected. So, a very small ratio of hydrogen (1%) was added to argon at atmospheric pressure and flowed at a rate of 40 sccm. The discharge was operated in both DC and short pulse modes.

5.4.1 DC Electron Density Measurements

In DC measurements, the electron density dependence on current was measured. The operating pressure was maintained at atmospheric and the current was varied in the range of 3 to 11 mA. The Hydrogen line was captured using the ICCD camera and the best fit was a Lorentzian profile. The Stark broadening is measured as the difference of the FWHM of the hydrogen line and the FWHM of the mercury line. Figure (5.22) shows a comparison between the mercury line and a DC hydrogen line. In this figure, it is clear that the hydrogen line is wider than the mercury line. The electron density can be obtained by using the following relation [68]:

$$n_e = 1.03*10^{16} \left(\Delta\lambda(nm)\right)^{1.488} \quad cm^{-3} \qquad (5.6)$$

where $\Delta\lambda$ is the Stark broadening FWHM. In the current range from 3 to 11 mA, the electron density increases linearly, as can be seen in figure (5.23), and was in the range of 10^{15} /cm^3. While the current was increased by almost a factor of 4, the electron density increased by only a factor of 1.5. This can be explained from the following equation:
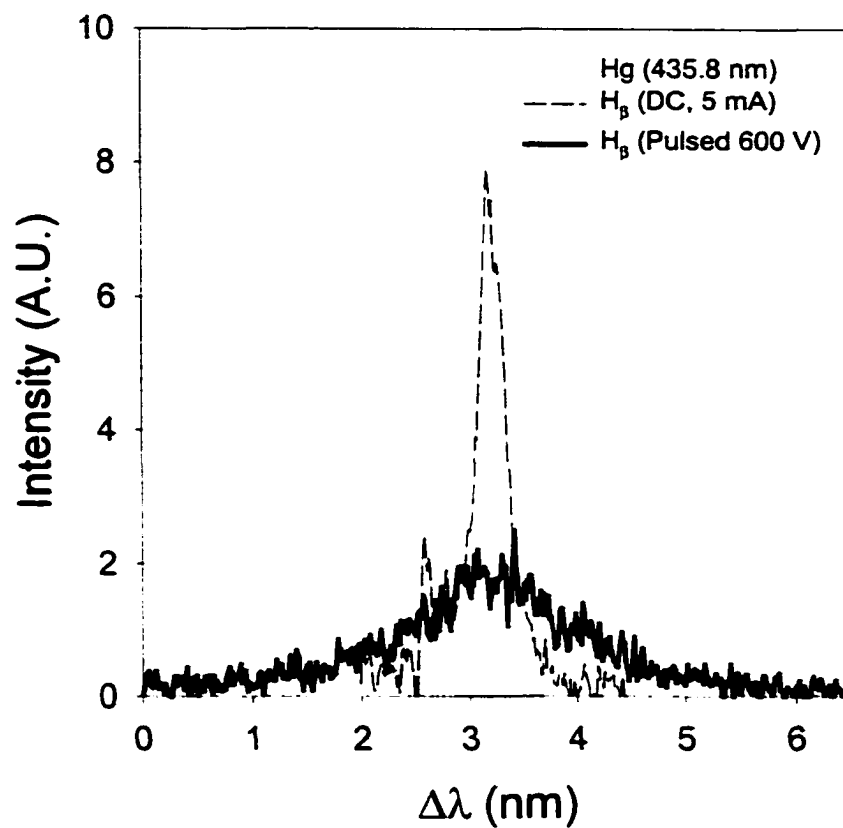
Figure (5.22) A system profile is obtained by measuring the mercury lamp line at 435.8 nm. For H_β line at 486.1 nm was recorded for both DC and pulsed measurements to obtain the Stark broadening and consequently the electron density.

$$I = e \cdot n \cdot v \cdot A \hspace{4cm} (5.7)$$

where I is the current, e the electron charge, n the electron density, v the drift velocity, and A is the area. The drift velocity is constant since the discharge voltage is constant. From this the current is proportional to both the electron density and the area, which was found to be linearly increasing also with increasing current and as could be seen from figure (5.23).

5.4.2 Pulsed Electron Density Measurements

For pulsed operation, a 10 ns pulse was applied to 10 mA DC discharge at atmospheric pressure and a time resolved electron density was measured. For a pulse voltage of 600 V, the electron density increased to 5×10^{16} cm^{-3} and decayed exponentially with a time constant of 150 ns due to loss process, as can be seen in figure (5.24). This increase in the electron density as a result of applying the 10 ns pulse confirms the importance of these "ns" pulses for VUV excimer emission, since the density of excited atom increased by increasing the electron density.
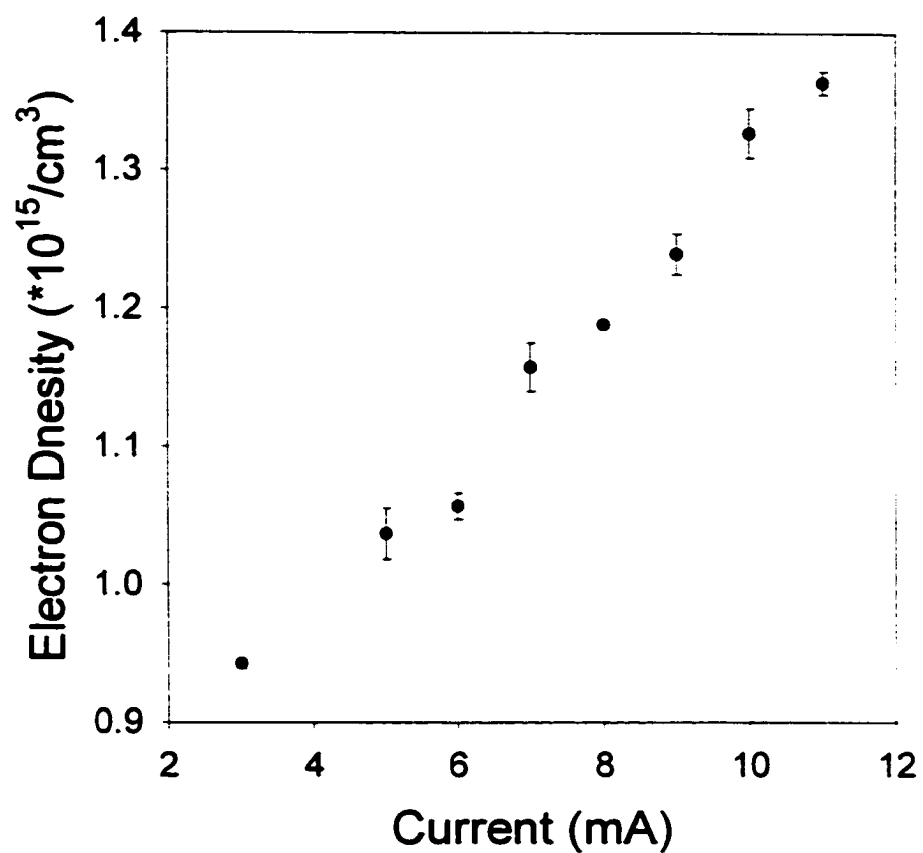
Figure (5.23) Electron density for DC MHCD in atmospheric pressure argon. The electron density increased linearly with increasing current. The electron density was in the range of 10^{15} /cm^3.
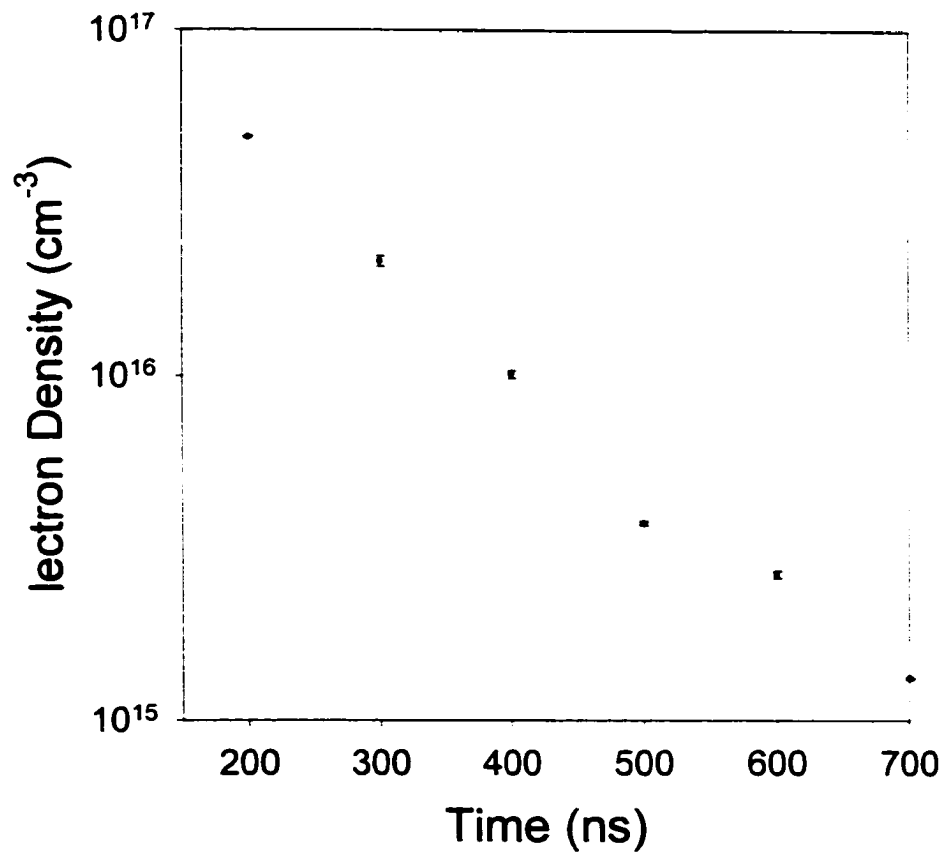
Figure (5.24) Time resolved electron density measurements for "ns" pulsed operation of atmospheric pressure MHCD in argon for a pulse voltage of 600 V and a DC current of 10 mA. The electron density decayed exponentially with a time constant of 150 ns.

CHAPTER VI

DISCUSSION

6.1 From MHCD to Micro-Surface Discharge

VUV images of the excimer source have shown that the source size is dependent on both current and pressure, as can be seen from figures (5.2) and (5.3). At low current, the discharge represents a Townsend discharge where the discharge is inside the hole covering part or all of the cathode area depending on how low the current is. This Townsend discharge is observed in the positive resistive region of the I-V characteristics. Increasing the current beyond this range, the discharge starts to expand over the cathode surface. Increasing the current at a constant pressure, the discharge switches to a normal glow discharge, where the voltage stays constant with increasing current, and the diameter of the excimer source increase with increasing current and decrease with increasing pressure. For a normal glow discharge, the current density is independent of the current:

$$J = I/A = \text{constant} \tag{6.1}$$

Hence, the area of the discharge is directly proportional to the current at a constant pressure. The spatially averaged current density was measured to be 0.3 A/cm^2 in 400 Torr xenon. While the current density is independent of the current it is proportional to the square of the pressure [64] at constant current

$$J = I/A = Cp^2 \tag{6.2}$$

and the area is inversely proportional to the square of pressure and would decrease with increasing pressure.

Side-on images in 200 Torr xenon have shown the thickness of the cathode fall and negative glow layers to be in the range of 100 μm. The cathode fall thickness and negative glow length are dependent on the gas, gas pressure, and electrode material. The cathode fall thickness, d_n, in a normal glow discharge is given by [36]

$$d_n = 3.76 \frac{\ln(1 + 1/\gamma)}{Ap} \qquad (6.3)$$

where γ is the secondary electron emission coefficient, p is the pressure, and A is a constant. In argon discharge at a discharge voltage of 200 V and pressure of 1 Torr, the negative glow length was measured to be 1 cm and is inversely proportional with pressure [36]. Hence, for a 200 Torr argon gas discharge with aluminum as the cathode γ=0.12 and A=13.6 /cm.Torr and consequently d_n=30 μm, and the negative glow length is 50 μm, totaling 80 μm. Data of aluminum and argon were used to demonstrate that the measured discharge thickness is close to theoretical values.

Being a normal glow discharge is not surprising since experiments and modeling of hollow cathode discharge have shown that there exists an upper limit of the pD product of 5 Torr cm for a stable discharge operation inside the cathode hole [33,34]. When pD value exceeds the limit the coupling through pendel electrons ceases to exist and the discharge spreads over the cathode surface. Experiments of MHCD in argon with pressure up to 896 Torr and a hole diameter of 200 μm have shown a stable discharge inside the hole up to a

pressure of 250 Torr (pD=5 Torr cm) and any further increase in the pressure leads to a filamentary discharge outside the hole [34].

In our experiment, the hole diameter used is 100 μm, and the pressure is up to atmospheric in xenon (pD=7.6 Torr cm) and 1100 Torr in argon (pD=11 Torr cm). The pD product in this case exceeds the upper limit of MHCD, and the discharge acts as a normal glow discharge.

6.2 Spatial Distribution of Current Density in The Normal Glow

In equilibrium pulsed operation of low-pressure xenon discharge, the excimer intensity close to the cathode opening was found to be lower than at further distances as in figure (5.17) (VUV image), which can be explained from the following: For a constant transverse (with respect to the cathode surface) current density, shown in figure (6.1), the radial current density increases with reduced distance, r, from the cathode opening according to [63]

$$J_r(r) = \frac{J_t}{2t}(r - \frac{r_o^2}{r})$$

(6.4)

where r_o is the maximum radius of the plasma layer. This means that the gas temperature due to Joule heating is also expected to increase with reduced distance to the cathode hole. This temperature increase is detrimental for excimer emission [13]. Due to the expected higher electron density in the higher temperature plasma, recombination radiation losses, which vary with the square of the electron density, are more likely in this area. In addition, the increased gas temperature close to the cathode hole might, as a secondary effect, cause an increase in cathode temperature and consequently increased thermal emission of electrons from the cathode in addition to electron emission caused by ion

impact. Thermal emission is known to cause a reduction in cathode fall voltage, and consequently a reduction in the number of high-energy electrons, required for the generation of the excimer precursors, as can be seen from the lower excimer intensity close to the cathode hole in figure (5.17).

6.3 Discharge Stability

High-pressure glow discharge in a plane electrode configuration has been one of the major issues due to the increased thermal instabilities at high pressure. The onset of these instabilities is dependent on the current and the current density of the discharge, whether it is higher or lower than the threshold value. It is more dominant at high pressure due to the previously mentioned dependence of the current density on the square of the pressure. These thermal instabilities are mechanisms perturbing homogeneous discharges at high pressures and currents in atomic and molecular gases [64,46,69]. They result in discharge contraction and in the formation of current filaments in which the degree of ionization and the gas temperature are higher than ordinary. As a result of this high temperature, the local atom (molecule) (N) concentration decreases, and the reduced electric field (E/N) increases. An increase in the reduced electric field increases the ionization rate and consequently the electron density and the current density. This increases the joule heating and leads to a higher temperature, and the process is repeated. This positive feedback results in increasing the current density in the discharge and a glow-to-arc transition. In microhollow cathode discharge, this glow-to-arc transition was not observed and a normal glow discharge was maintained for the current and pressure range of

operation. This is mainly due to the current range of operation in both DC and equilibrium pulsed operation, which didn't exceed 80 mA. Thermal instabilities require a relatively high current, which would allow generating electrons through thermal heating and forming a hot cathode spot. A normal glow discharge with current below 100 mA is stable since the joule heating is not high enough to cause instabilities [70]. When the current is in the range of 100 to 200 mA a contracted channel with a confined radius tries to form and increases the current density at the cathode surface forming a hot spot. But since the current is not high enough to support this channel it switches back to a normal glow discharge. For current higher than 200 mA, a glow-to-arc transition occurs and an arc discharge is formed. Since the current in MHCDs didn't exceed 80 mA, no glow-to-arc transition was observed. As for the case of non-equilibrium pulsed operation, a glow-to-arc transition would be possible due to the high current, in the range of hundreds of mA, but this transition wasn't established because of the short pulse width which doesn't allow for gas heating during the pulse.

6.4 Non-Equilibrium Pulsed Operation

6.4.1 Electron Energy

Excimer formation requires high-energy electrons, and it has been shown from the spectral measurements in both xenon and argon discharge that there are electrons with high energy enough to excite the gas atoms, precursors for excimer formation. In equilibrium pulsed operation, the efficiency stayed constant as in the DC case, although the intensity increased.
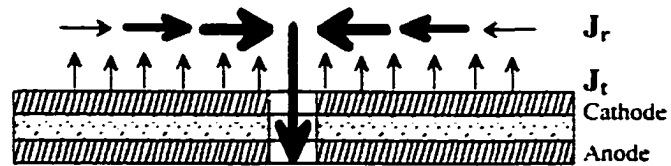
Figure (6.1) Cross-section of microhollow electrodes, with the discharge plasma extending over the cathode surface. The arrows indicate the transverse and radial current density, J_t, J_r, in the plasma. The instabilities current diffuses in the negative glow.

However, in non-equilibrium pulsed operation in xenon, a strong increase in optical power and the increase in efficiency was observed, which can be explained by nonequilibrium effects in the discharge plasma. Calculations and measurements in air plasmas with similar short pulses applied indicate that the nanosecond pulses cause electron heating without affecting the gas temperature, which would shift the electron energy distribution function (EEDF) to higher energies, as shown in figure (6.2) [48].

In order to obtain such an electron heating effect, the pulse duration should be less than the electron relaxation time. This allows us to heat the electrons, without heating simultaneously the gas, and consequently reduces the probability for glow-to-arc transition. The relaxation time of electron, τ, to transfer the energy to the atoms is given by [69]

$$\tau = \frac{1}{\delta v_m}$$ (6.5)

where $\delta = 2m_e/M$ and v_m is the effective collision frequency for momentum transfer. For argon at atmospheric pressure $\delta = 6.86 \cdot 10^{-6}$ and $v_m = 4.03 \cdot 10^{12}$ s^{-1} [69]. In this case, the relaxation time in atmospheric pressure argon is $\tau = 36$ ns.

Pulsing the discharge with pulses with pulse duration shorter than τ allows for heating the electrons and minimum energy transfer to the gas atoms during the time of the pulse application. Applying the pulse for such a short time guarantees therefore that glow to arc transition can be avoided because gas heating occurs after the voltage pulse is applied.
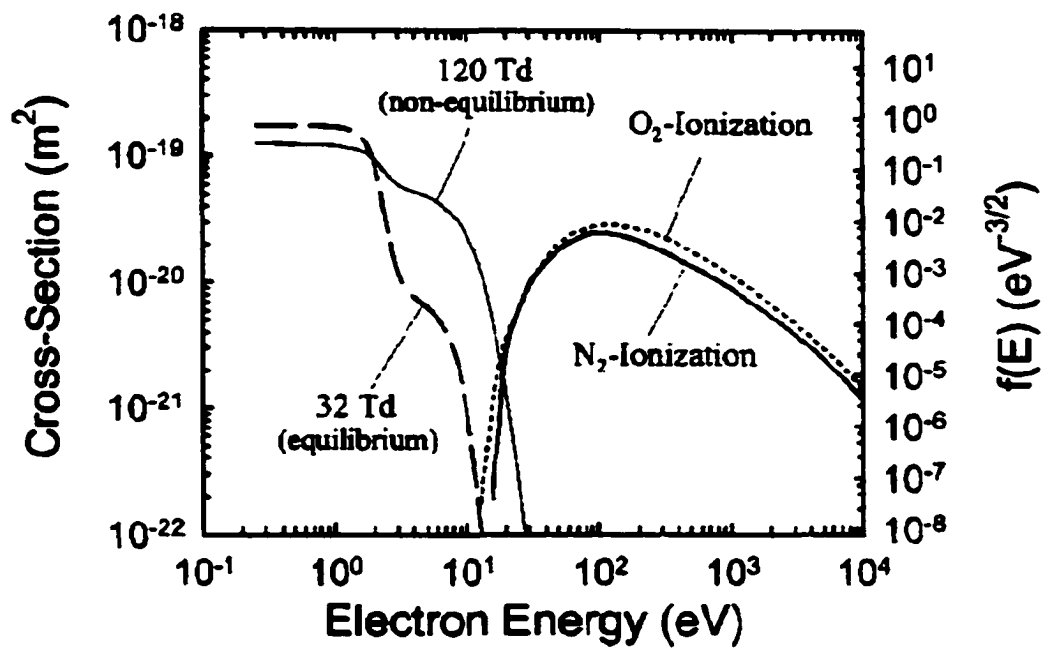
Figure (6.2) Ionization cross section, and the steady state (dashed) and transient (solid) EEDF for electrons in an atmospheric pressure air discharge [48].

6.4.2 Excimer Emission In Non-Equilibrium Pulsed Operation

The observed temporal response of the excimer emission to the 20 ns pulse (figure (5.18)) is consistent with experimental and theoretical results obtained on barrier discharges. A model by Adler et. al [71] was used to simulate excimer formation and decay. In his model, Adler presented the different reactions that take place in excimer formation and decay. The main reactions that control the process in barrier discharges, as well as in MHCDs, can be summarized in the following equations:

$$Xe(^3P_2) + 2Xe(^1S_0) \xrightarrow{k_2} Xe_2^*(1_u, O_u^-, v \gg 0) + Xe(^1S_0) \qquad (6.6)$$

where a three-body collision takes place with the $^3P_2$ meta stable state forming the excimer molecule. These excimer states either will decay radiatively (1st continua):

$$Xe_2^*(1_u, O_u^-, v \gg 0) \xrightarrow{\tau_2} Xe_2(O_g^*) + h\nu(\lambda_{max} = 151\,nm) \qquad (6.7)$$
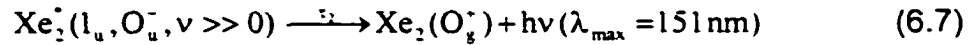
or will go through a vibrational relaxation:

$$Xe_2^*(1_u, O_u^-, v \gg 0) + Xe(^1S_0) \xrightarrow{k_4} Xe_2^*(1_u, O_u^-, v \approx 0) + Xe(^1S_0) \qquad (6.8)$$
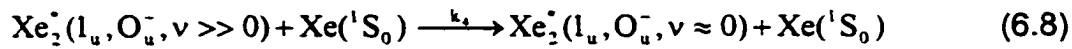
The low vibrational states decays radiatively in the 2nd continua:

$$Xe_2^*(1_u, O_u^-, v \approx 0) \xrightarrow{\tau_4} Xe_2(O_g^*) + h\nu(\lambda_{max} = 172\,nm) \qquad (6.9)$$
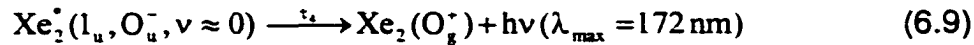
At high electron energy and density electron ion recombination processes and subsequent relaxation processes have to be taken into consideration since it can feed the excimer levels via the P and S levels:

$$Xe^*(^2P_J) + 2Xe \xrightarrow{k_5} Xe_2^* + Xe$$
$$Xe_2^*(^2\Sigma) + e^- \xrightarrow{\alpha_R} Xe^{**} + Xe(^1S_0) \qquad (6.10)$$
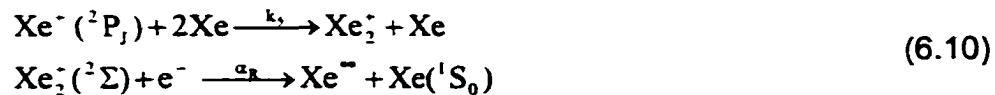
In this system a quasi-neutrality was assumed and hence:

$$n_e = n_{Xe^-} + n_{Xe_2^+}$$

(6.11)

From the above reaction, a set of differential equations had to be solved [71]:

$$\frac{d}{dt}n_{Xe^-} = -(k_1 p^2)n_{Xe^-}$$

$$\frac{d}{dt}n_{Xe_2^+} = (k_1 p^2)n_{Xe^-} - \alpha_R(t)n_{Xe_2^+}(n_{Xe_2^+} + n_{Xe^-})$$

$$\frac{d}{dt}n_{Xe(^3p_2)} = \alpha_R(t)n_{Xe_2^+}(n_{Xe_2^+} + n_{Xe^-}) - (k_2 p^2)n_{Xe(^3p_2)}$$

(6.12)

$$\frac{d}{dt}n_{Xe(1_u,v>>0)} = (k_2 p^2)n_{Xe(^3p_2)} - (k_4 p)n_{Xe(1_u,v>>0)} - \tau_2^{-1}n_{Xe(1_u,v>>0)}$$

$$\frac{d}{dt}n_{Xe(1_u,v=0)} = (k_4 p)n_{Xe(1_u,v>>0)} - \tau_4^{-1}n_{Xe(1_u,v=0)}$$

where p is the pressure, α_R is the recombination coefficient, k_2 and k_4 are rate coefficient and τ_2 and τ_4 are the life times of the excimer states. These differential equations included the rate equations for xenon atomic ions (Xe^+), xenon molecular ions (Xe^+_2), xenon metastable atoms ($Xe(^3p_2)$), high vibrational levels excimer ($Xe(1_u,v>>0)$) corresponding to the first continuum emission and low vibrational levels excimer ($Xe(1_u,v\approx0)$) corresponding to the second continuum emission; the initial conditions for these equations need to be known. At this point we had to guess the initial values, since measurements of the densities of the various excited and ionized species are not yet available for dc operation. For a 3 mA DC current, 400 Torr xenon the estimated values were $Xe^+=2*10^{14}$ /cm^3, $Xe^+_2=2*10^{13}$ /cm^3, $Xe(^3p_2)=4*10^{13}$ /cm^3, $Xe(1_u,v>>0)= 4*10^{11}$ /cm^3, and $Xe(1_u,v\approx0)=4*10^{11}$ /cm^3. The results provide consequently only qualitative information and are shown in figure (5.18) (dashed line). They indicate that the rise of the excimer emission is due to three-body collision, forming the dimer, and

the fact that the fall time is determined by dimer recombination and radiative emission.

Applying a 10 ns pulse to argon discharge increases the intensity six times over the DC value, while in xenon it was more than two orders of magnitude. This is because the threshold of the excitation cross section of argon (11.55 eV) is higher than that of xenon (8.32 eV), so the excitation rate in xenon is expected to be higher than that in argon.

Applying short pulses with width in the range of 10-20 ns also increased the electron density in the discharge. In the DC operation, the electron density was in the range of 10^{15} /cm^3. Applying these pulses increased the electron density by a factor of 50 to $5 \cdot 10^{16}$ /cm^3 and decayed exponentially with a time constant of 150 ns. This increase in the electron density results also in increasing the excimer intensity in a non linear relation since in argon the electron density increased by a factor of 50 while the intensity increased by only a factor of six.

Adler's model was used to calculate the excimer state density and its dependence on the electron. The same initial conditions as mentioned above were used, and only the initial condition for atomic and molecular ions were changed corresponding to the change of the electron density. The model results showed a linear dependence of the excimer density on the electron density, as shown in figure (6.3).
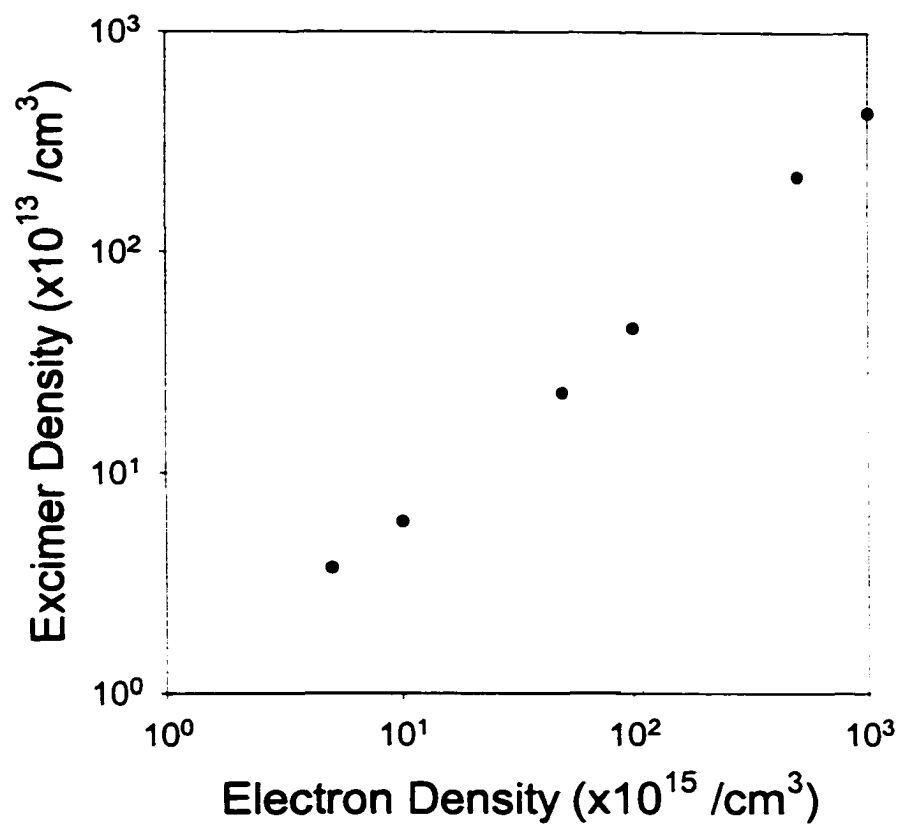
Figure (6.3) Dependence of the excimer state density on the electron density in non-equilibrium pulsed operation.

6.5 Effect Of Contamination on Excimer Emission

Impurities cause reduction of excimer formation since the presence of impurities reduces the generation of the excited states. Another effect of the presence of impurities is the collisional quenching of the excited rare gas atoms, the precursors of the excimer. Possible sources of these impurities are a small leakage in the discharge chamber, water vapor remnant, deposition on the cathode surface, or even produced by the dielectric layer (Al_2O_3) and silver epoxy due to the high gas temperature. This is clear in figure (5.6) where atomic lines of oxygen and hydrogen were detected indicating the presence of water vapor in the chamber. Also some carbon lines were observed, and the source might be the silver epoxy since it is an organic compound. The effect of impurities can be seen by comparing figures (5.6) and (5.11). In figure (5.6) when the discharge was operated in static argon, due to the existence of oxygen, hydrogen, nitrogen, and carbon impurities the excimer emission decreased. On top of the argon excimer continuum, an oxygen triplet was observed. The reduction in excimer intensity and the excitation of the oxygen triplet is assumed to be due to resonant energy transfer from Ar_2^* excimers with an energy in excess of 9.54 eV, corresponding to wavelengths shorter than 130.2 nm, or possibly also from excited argon atoms at 13.2 eV, which serve as precursors for excimer formation and by increasing the oxygen concentration the excimer continuum disappeared. This effect is not totally unacceptable since it can be used for generating high intensity low wavelength emission, which can be used for advanced photolithography. Because of the small concentration of oxygen in argon, the

reabsorption of the 130.4 nm radiation in the gas mixture is presumably negligible for distances relevant for such an application, typically on the order of centimeter. Looking at figure (5.11) where the gas discharge was achieved in a flowing gas, it can be seen that the impurity lines almost disappeared, and the excimer continuum intensity increased. This elimination of impurities increased the excimer efficiency from 1% (static) to 6% (flow). Another effect of the presence of impurities is collisional quenching of the excited rare gas atoms, the precursors of the excimer.

CHAPTER VII

Summary

Two conditions have to be satisfied for excimer formation: a sufficient percentage of the electron with high-energy that excites the gas atoms and high pressure so that three body collisions between the excited atoms and two ground state atoms forming the excimer molecule would be more favorable. In this dissertation, two rare gases have been studied for excimer radiation: xenon at 172 nm and argon at 127 nm. Microhollow cathode discharges are one of the configurations that can be used for excimer generation. The high-energy electrons in this configuration are established by accelerating the electron in the cathode fall, and due to the pendel effect, the ionization and excitation rate would increase in the negative glow region increasing the possibility of excimer formation.

Spatial distribution measurements of VUV radiation from MHCDs in xenon and argon showed that the source size increases with increasing current and decreases with pressure. In the case of MHCD in xenon, it was found that at a constant pressure of 400 Torr, the average current density stays constant at 0.3 A/cm^2, while at constant current it is proportional to the square of the pressure. These two relations are typical for a normal glow discharge. In addition, VUV intensity profiles in DC operation of MHCD in xenon showed an increasing radiant emittance with increasing pressure up to 2 W/cm^2 at atmospheric pressure and a current of 3 mA.

In DC operation, the current was limited to 10 mA to avoid thermal damage of the sample, so "ms" pulses were applied to the discharge to enable increasing the current without increasing the average power. Pulsing the discharge enabled increasing the current to 80 mA, and the intensity was linearly increasing with increasing current up to 1.25 W at 400 Torr at a constant voltage. In these steady state measurements the efficiency stayed constant at 7% similar to the DC value.

By applying short pulses with width in the ns range to the discharge, electrons are heated to higher energies without heating the plasma simultaneously. The pulse width was in the range of 10-20 ns, which is shorter than the time constant for glow to arc transition. Applying "ns" pulses to DC MHCDs in xenon resulted in increasing the intensity exponentially with increasing pulse voltage to 2.75 W and the efficiency linearly to 20% at a pulse peak pulse voltage of 750 V. Using the VUV images and power measurements, the radiant emittance was found to increase from 2 W/cm^2 in DC operation to 15.2 W/cm^2 in pulsed operation.

A power measurement of MHCD in flowing argon showed a linearly increasing intensity with increasing current and increases with increasing pressure. The DC efficiency of MHCD in flowing argon at a flow rate of 40 sccm, a pressure of 1100 Torr, and a current of 3 mA was measured to be 6%, which is six times that of static argon operation.

"ns" pulsed operation in flowing argon showed a slight increase in the intensity of about six times the DC level when a pulse was applied to the DC

discharge with a pulse width of 10 ns. The intensity increased with increasing pulse voltage until a breakdown occurred associated with a high current pulse. In these measurements, the efficiency was found to be equal to or lower than the DC efficiency at 5-6%.

Electron density of 10^{15} /cm^3 was measured in DC flowing argon at atmospheric pressure. By pulsing the discharge with a 10 ns pulse the density increased to 5.10^{16} /cm^3 and decayed with a time constant of 150 ns.

REFERENCES

1. H. Kumagai and M. Obara, Jpn. J. Appl. Phys. Part 2- Lett. **28**, L2228 (1989).

2. U. Kogelschatz, B. Eliasson, and H. Esram, Abb Review, 21 (1991).

3. A. El-Habachi and K.H. Schoenbach, Appl. Phys. Lett. **73**, 885 (1998).

4. A. El-Habachi and K.H. Schoenbach, Appl. Phys. Lett. **72**, 22 (1998).

5. A. El-Habachi, W. Shi, M. Moselhy, R.H. Stark, and K.H. Schoenbach, J. Appl. Phys. **88**, 3220 (2000).

6. P. Kurunczi, J. Lopez, H. Shah, and K. Becker, Int. J. Mass Spectrom. **205**, 277 (2001).

7. A.K. Shuaibov, A.I. Minya, and A.I. Dashchenko, Tech Phys. **46**, 1582 (2001).

8. Zhang Jun-Ying and I.W. Boyd, Appl. Phys. Lett. **71**, 2964 (1997).

9. UVP data sheet, www.uvp.com/penary/html/penary.html.

10. UV Process Supply Inc., www.uvlamp.com/techart/shortarc.htm.

11. U. Kogelschatz, *Proc. XX Int. Conf. on Phenomena in Ionized Gases (ICPIG)*, Pisa, 1991, p 1.

12. R.P. Mildren and R.J. Carman, J. Phys. D: Appl. Phys. **34**, L1 (2001).

13. J.D. Ametepe, J. Diggs, D.M. Manos, and M.J. Kelley, J. Appl. Phys. **85**, 7505 (1999).

14. E. Nasser, *Fundamentals of Gaseous Ionization and Plasma Electronics*, Wiley-Interscience, New York, 1971.

15. A. D. White, J. Appl. Phys. **30**, 711 (1959).

16. W. Shi, R.H. Stark, and K.H. Schoenbach, IEEE Trans. Plasma Science **27**, 16 (1999).

17. M. Krauss and F.H. Mies, *Topics in Applied Physics: Excimer Lasers* **30**, edited by Ch. K. Rhodes, Springer-Verlag, New York, 1984, Chapter 2.

18. U. Kogelschatz, Appl. Surf. Sci. **54**, 410 (1992).

19. B. Gellert and U. Kogelschatz, Appl. Phys. B **52**, 14-21 (1991).

20. D.C. Lorents, Physica **82C**, 19 (1976).

21. Charles W. Werner, Edward V. George, Paul W. Hoff, and Charles K. Rhodes, IEEE J. Quantum Electronics **13**, 769 (1977).

22. K.S. Gochelashvili, A.V. Dem'yanov, I.V. Kochetov, and L.R. Yangurazova, Laser Physics **3**, 140 (1993).

23. P. Moutard, P. Laporte, J. L. Subtil, N. Damany and H. Damany, J. Chem. Phys. **88**, 7485 (1988).

24. B. Schneider and J. S. Cohen, J. Chem. Phys. **61**, 3240 (1974) [Ref. 3.3].

25. N. Thonnard and G. S. Hurst, Phys. Rev. A **5**, 1110 (1972).

26. R. Bocique and P. Mortier, J. Phys. D **3**, 1905 (1970).

27. J. W. Keto, R. E. Gleason and G. K. Walters, Phys. Rev. Lett. **33**, 1375 (1974).

28. T. Oka, K. Raama Rao, J. Redgath and R. Firestone, J. Chem. Phys. **61**, 4740 (1974).

29. D. J. Eckstrom, H. H. Nakano, D. C. Lorents, T. Rothem, J. A. Betts, M. E. Lainhart, D. A. Dakin and J. E. Maenchen, J. Appl. Phys. **64**, 1679 (1988).

29a. A.P. Vitlos and H.J. Oskam, Phys. Rev. A **8** 1860 (1973).

29b. A.K. Bhattacharya, Appl. Phys. Lett. **17**, 521 (1970).

29c. C.W. Werner, E. Zamir, and E.V. George, Appl. Phys. Lett. **29**, 236 (1976).

29d. Y.J. Shiu, M.A. Biondi, and D.P. Sopler, Phys. Rev A **15**, 494 (1977).

29e. P.R. Timpson and J.M. Anderson, Can. J. Phys. **48**, 1817 (1970).

29f. J.H. Kolts and D.W. Setser, J. Chem. Phys. **68**, 4848 (1978).

29g. T.D. Bonfield, F.H.K. rambow, G.K. Walters, M.J. McCusker, D.C. Lorents, and R.A. Gutcheck, J. Chem. Phys. **72**, 2914 (1980).

29h. D.L. Huestis, in D.C. Lorents, D.J. Eckstrom, and D.L. Huestis, Report No. MP 73-2, Stanford Research Institute, Menlo Park, CA (September, 1973) (unpublished).

29i. T.N. Rescigno, A.U. Hazi, and A.E. Orel, J. Chem. Phys. **68**, 5283 (1978).

29j. E. Zamir, C.W. Werner, W.P. Lapatovich, and E.V. George, Appl. Phys. Lett. **27**, 56 (1975).

30. G. Schaefer and K.H. Schoenbach, *Physics and applications of pseudo sparks*, Plenum Press, New York, 1990.

31. P. Gill and C. E. Webb, J. Phys. D: Appl. Phys. **10**, 299 (1977).

32. H. Eichorn, K.H. Schoenbach, and T. Tessnow, Appl. Phys. Lett. **63**, 2481 (1993).

33. A. Fiala, L.C. Pitchford, and J.P. Boeuf, *Proc. XXII Int. Conf. on Phenomena in Ionized Gases*, Hoboken, 1995, Contr. Papers 4, 191.

34. Karl H. Schoenbach, Ahmed El-Habachi, Wenhui Shi, and Marco Ciocca, Plasma Sources Science and Technology, **6**, 468 (1997).

35. F. W. Aston, Proc. R. Soc. A **79**, 80 (1907).

36. J. D. Cobine, *Gaseous Conductors*, Dover Publications Inc., New York, 1958.

37. K.H. Schoenbach, R. Verhappen, T. Tessnow, F. E. Peterkin, and W. W. Byszewski, Appl. Phys. Lett. **68**, 13 (1996).

38. A. El-Habachi, Ph.D. Dissertation, Old Dominion University, 1998.

39. K.H. Schoenbach, A. El-Habachi, M.M. Moselhy, W. Shi, and R.H. Stark, Physics of Plasmas **7**, 2186 (2000).

40. P. Kurunczi, H. Shah and K. Becker, J. Phys. B: At. Mol. Opt. Phys., **32**, 651 (1999).

41. J.W. Frame, D.J. Wheeler, T.A. DeTemple, and J.G. Eden, Appl. Phys. Lett. **71**, 1165 (1997).

42. J.W. Frame and J.G. Eden, Electronics Lett. **34**, 1529 (1998).

43. L.D. Biborosch, O. Bilwatsch, S. Ish-Shalom, E. Dewald, U. Ernst, and K. Frank, Appl. Phys. Lett. **75**, 3926 (1999).

44. U. Ernst, K. Frank, and W. hartmann, *Conf. Record IEEE Intern. Conf. Plasma Science*, New Orleans, LA, 2000, 112.

45. K. Frank, U. Ernst, I. Petzenhauser, and W. hartmann, *Conf. Record IEEE Intern. Conf. Plasma Science*, Las Vegas, NV, 2001, 381.

46. E.E. Kunhardt and L. Luessen, *Electrical Breakdown and Discharges in Gases*, Plenum Press, New York, 1981.

47. Karl H. Schoenbach, Ahmed El-Habachi, Mohamed M. Moselhy, Wenhui Shi, and Robert H. Stark, Physics of Plasmas **7**, 2186 (2000).

48. Robert H. Stark and Karl H. Schoenbach, J. Appl. Phys. **89**, 3568 (2001).

49. IXYS data sheets.

50. J. Deng, R.H. Stark and K.H. Schoenbach, *Conf. Record of 24th Int. Power Modulator Symp.*, Norfolk, VA, 2000, p 47.

51. W. James Sarjeant, and R. E. Dollinger, *High Power Electronics*, Tab Books Inc., Blue Ridge Summit, PA, 1989, Chapter3.

52. McPherson manual for 0.2 m monochromator model 234/302.

53. Hamamatsu data sheets.

54. I.H. Hutchinson, *Principles of Plasma Diagnostics*, Cambridge Univ. Press, Cambridge, UK, 1987.

55. International Radiation Detectors data sheets.

56. Acton Research data sheets.

57. A. El-Habachi, M. Moselhy, and K.H. Schoenbach, *Bull APS (GEC)*, Vol. 44, October 1999, LR2 2, p. 67.

58. A. El-Habachi, M. Moselhy, A. El-Dakroury and K.H. Schoenbach, *Conf. Record 1999 IEEE Intern. Conf. Plasma Science*, Monterey, CA, Abstract 6A01, p. 248.

59. M. Moselhy, A. El-Habachi, W. Shi, R.H. Stark, and K.H. Schoenbach, *Bull APS (GEC)*, Vol. 45, October 2000, QF1 4, p. 70.

60. M. Moselhy, R.H. Stark, K.H. Schoenbach, and U. Kogelschatz, Appl. Phys. Lett. **78**, 880 (2001).

61. M. Moselhy, A. El-Habachi, and K.H. Schoenbach, *Bull APS (GEC)*, Vol. 44, No. 4, October 1999, ETP4 58, p. 29.

62. A. El-Habachi, M. Moselhy, R.H. Stark, and K.H. Schoenbach, *Conf. Record, IEEE Intern. Conf. Plasma Science*, New Orleans, 2000, 6A01-02, p. 254.

63. Mohamed Moselhy, Wenhui Shi, Robert H. Stark, and Karl H. Schoenbach, IEEE Trans. Plasma Sci. **30**, 198 (2002).

64. E.E. Kunhardt, IEEE Trans. Plas. Sci. **28**, 189 (2000).

65. Mohamed Moselhy, Wenhui Shi, Robert H. Stark, and Karl H. Schoenbach, *Conf. Record, IEEE PPPS*, Las Vegas, 2001, O1I8, p.247.

66. Mohamed Moselhy, Wenhui Shi, Robert H. Stark, and Karl H. Schoenbach, *Bull APS (GEC)*, **46**, October 2001, ET1 5, p. 28.

67. M. Moselhy, W. Shi, R. H. Stark, and K. H. Schoenbach, Appl. Phys. Lett. **79**, 1240 (2001).

68. C. Fleurier, A. Sanba, D. Hong, J. Mathias, and J.C. Pellicer, J. de Physique, **49**, 141 (1988).

69. Yu.P. Raizer, *Gas Discharge Physics*, Springer-Verlag, New York, 1997.

70. Private communication with Dr. Yu. D. Korolev, Institute of High Current Electronics, Russia.

71. F. Adler and S. Müller, J. Phys. D **33**, 1705 (2000).

APPENDIX

A. Kinetic Model for Xenon

A complete list of the kinetic processes in xenon and the rates of different reactions are given in table A.1 [29].

TABLE A.1 Kinetic model of xenon.

Reaction	Rate[a]	Reference
1. $Xe^* + 2Xe \rightarrow Xe_2^* + Xe$	$2 \times 10^{-31}(300/T_e)^{1/2}$	29a, 29b
2. $Xe_2^+ + 2Xe \rightarrow Xe_2^* + Xe$	$6 \times 10^{-32}(300/T_e)^{1/2}$	29c
3. $Xe_2^+ + e \rightarrow Xe^{**} + Xe$	$2.3 \times 10^{-7}T_e^{-0.5}$	29d
4. $Xe_2^+ + e \rightarrow Xe^{**} + 2Xe$	$1 \times 10^{-7}T_e^{-0.5}$	29c
5. $Xe^{**} + 2Xe \rightarrow Xe_2^* + Xe$	$5 \times 10^{-32}(300/T_e)^{1/2}$	29
6. $Xe_2^* \rightarrow Xe^* + Xe$	1×10^7	29
7. $Xe_2^* + Xe \rightarrow Xe^* + 2Xe$	$1 \times 10^{-11}(T_e/300)^{1/2}$	29
8. $Xe^* + 2Xe \rightarrow Xe_2^{*'} + Xe$	$4.4 \times 10^{-32}(300/T_e)^{1/2}$ [b]	29e, 29f
9. $Xe^* + 2Xe \rightarrow Xe_2^{*'} + Xe$	$2 \times 10^{-33}(300/T_e)^{1/2}$ [b]	29g
10a. $e + Xe_2^{*'} \rightarrow e + Xe_2^{*'}$	1.8×10^{-8}	29 (x 0.1)
10b. $e + Xe_2^{*'} \rightarrow e + Xe_2^{*'}$	4.9×10^{-8}	29 (x 0.1)
11a. $Xe_2^{*'} + Xe \rightarrow Xe_2^{*'} + Xe$	$4.6 \times 10^{-10}(T_e/300)^{1/2}$	29g
11b. $Xe_2^{*'} + Xe \rightarrow Xe_2^{*'} + Xe$	$1.2 \times 10^{-13}(T_e/300)^{1/2}$	29g
12. $Xe_2^{*'} \rightarrow 2Xe + h\nu$	2.1×10^7	29g
13. $Xe_2^{*'} \rightarrow 2Xe + h\nu$	1×10^7	29g
14. $Xe_2^{*'} + h\nu \rightarrow Xe_2^+ + e$	$2 \times 10^{-18} cm^2$	29h, 29i
15. $Xe_2^{*'} + h\nu \rightarrow Xe_2^+ + e$	$2 \times 10^{-18} cm^2$	29h, 29i
16. $2Xe_2^* \rightarrow Xe_2^+ + 2Xe + e$	8×10^{-11}	29j
17. $2Xe^* \rightarrow Xe^+ + Xe + e$	8×10^{-11}	29j
18. $Xe_2^* + e \rightarrow Xe_2^+ + 2e$	5×10^{-8}	29
19. $Xe^* + e \rightarrow Xe^+ + 2e$	2.7×10^{-8}	29
20. $Xe_2^* + e \rightarrow 2Xe + e$	4×10^{-9}	29 (x3)
21. $Xe^* + e \rightarrow Xe + e$	3×10^{-8}	29 (x3)
22. $Xe_2^* + e \rightarrow Xe^* + Xe + e$	2×10^{-7}	29
23. $Xe_2^* + e \rightarrow Xe_2^{*'} + e$	3×10^{-7}	29
24a. $Xe^* + e \rightarrow Xe^{*'} + e$	6×10^{-7}	29
24b. $Xe^* + e \rightarrow Xe^{*'} + e$	2×10^{-7}	29
25. $Xe^{**} \rightarrow Xe^* + h\nu$	$< 1 \times 10^6$	29
26. $Xe^{**} + e \rightarrow Xe^* + 2e$	2×10^{-6}	29
27. $Xe^* + e \rightarrow Xe^{**} + e$	3×10^{-7}	29
28. $Xe^{**} + e \rightarrow Xe^* + e$	8×10^{-7}	29
29. $Xe^{**} + h\nu \rightarrow Xe^* + e$	$1 \times 10^{-18} cm^2$	29h
30. $2Xe^{**} \rightarrow Xe^* + Xe + e$	1×10^{-9}	29j
31. $2Xe_2^* \rightarrow Xe_2^+ + 2Xe + e$	1×10^{-9}	29j
32. $Xe_2^+ + e \rightarrow Xe^* + Xe + e$	1×10^{-7}	29
33. $Xe_2^* + e \rightarrow Xe_2^+ + 2e$	6×10^{-8}	29
34. $Xe_2^* + h\nu \rightarrow Xe_2^+ + e$	$1 \times 10^{-18} cm^2$	29h

[a] Units are cm^3/s, cm^6/s, s^{-1}, or cm^2 (where noted) as appropriate.
[b] Xe^* includes the $6s'P_2$ and $6s'P_1$ states, which are assumed to be in statistical equilibrium.
[c] At $T_e = 1 eV$.

VITA
for
MOHAMED MOSELHY

DEGREES:

Doctor of Philosophy (Electrical Engineering), Old Dominion University, Norfolk, Virginia, August 2002.

Master of Science (Electrical Engineering), Alexandria University, Alexandria, Egypt, November 1997.

Bachelor of Science (Electrical Engineering), Alexandria University, Alexandria, Egypt, June 1993.

PROFESSIONAL CHRONOLOGY:

Department of Electrical Engineering, Old Dominion University, Norfolk, Virginia

> Graduate Research Assistant, September 1998- Present

Department of Electrical Engineering, Communication Section, Alexandria University, Alexandria, Egypt,

> Assistant Lecturer, March 1994- September 1998.

COURSES TAUGHT DURING THE LAST FIVE YEARS:

Electronic Circuits, Electronic Circuits lab, Circuit Design, Circuit Design Lab, Communication Systems, Modern Physics.

SCHOLARLY ACTIVITIES COMPLETED:

- "A Flat Glow Discharge Excimer Radiation Source," IEEE Trans. Plasma Sci. **30**, 198 (2002).
- " Vacuum Ultraviolet Spectroscopy of Microhollow Cathode Discharge Plasmas," Proc. SPIE Vol. **4460**, p. 239, Selected Research Paper on Spectroscopy of Nonequilibrium Plasma at Elevated Pressures, Vladimir N. Ochkin; Ed., 2002.
- "Xenon excimer emission from pulsed microhollow cathode discharges," Appl. Phys. Lett. **79**, 1240 (2001).
- "Resonant Energy Transfer from Argon Dimers to Atomic Oxygen in Microhollow Cathode Discharges," Appl. Phys. Lett. **78**, 880 (2001).
- "Series Operation of Direct Current Xenon Chloride Excimer Sources," J. Appl. Phys. **88**, 3220 (2000).
- "Microhollow Cathode Discharge Excimer Lamps," Physics of Plasmas **7**, 2186 (2000).